Journal Pre-proof

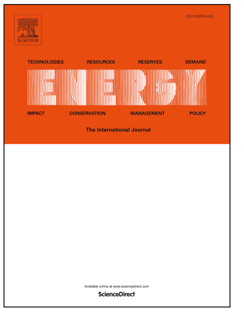

A novel thermal model for PV panels with back surface spray cooling

Piero Bevilacqua, Roberto Bruno, Antonino Rollo, Vittorio Ferraro

PII: S0360-5442(22)01304-4

DOI: https://doi.org/10.1016/j.energy.2022.124401

Reference: EGY 124401

To appear in: *Energy*

Received Date: 7 November 2021

Revised Date: 2 May 2022

Accepted Date: 28 May 2022

Please cite this article as: Bevilacqua P, Bruno R, Rollo A, Ferraro V, A novel thermal model for PV panels with back surface spray cooling, *Energy* (2022), doi: https://doi.org/10.1016/j.energy.2022.124401.

Piero Bevilacqua: Conceptualization, Methodology, Validation, Investigation, Formal analysis, Writing - Original Draft, Writing - Review & Editing, Visualization, Supervision, Project administration

Roberto Bruno: Investigation, Formal analysis, Writing - Review & Editing, Supervision, Project administration

Antonino Rollo: Conceptualization, Methodology, Software, Validation, Formal analysis, Data Curation, Writing - Review & Editing,

Vittorio Ferraro: Resources, Supervision

A novel thermal model for PV panels with back surface spray cooling

Piero Bevilacqua, Roberto Bruno, Antonino Rollo, Vittorio Ferraro*

*corresponding author: piero.bevilacqua@unical.it

Department of Mechanical, Energy and Management Engineering, University of Calabria, Ponte P. Bucci 46/C, ZIP 87036 Arcavacata di Rende, CS, Italy

Abstract

To improve the performances of Photovoltaic systems, water-based cooling systems have been considered as an interesting option. The study proposes a novel mono-dimensional thermal model that includes the modeling of the spray cooling phenomena on the back surface. The model was validated with data of an experimental setup with a PV panel equipped with two spray nozzles. The model, based on the energy balance method with a Finite Difference approach, can provide the thermal field across the panel thickness. Simulations were carried out over a large number of days in the summer period with a short time step (5 s). Results showed an average RMSE of 1.37 °C, RMSEP of 0.005 % and NSE of 96.5 % for the back surface temperature, and an average RMSE of 3.39 W, RMSEP of 0.36 % and NSE of 99.6 % for the electric power. A further assessment of the cooling phenomenon highlighted the contribution of sensible and latent energy exchanges to the panel energy balance. Finally, a comparison of the performances with a non-cooled Pv panel showed an average increase of 7.82% of the electric power in solar radiation peak hours and a reduction of 28.23 % of the average cell temperature.

Keywords

PV thermal modeling; Experimental validation; Cooling systems; Spray cooling thermal model

Nomenclature

A	Surface area [m²]
a	Estimated value from the model [°C or W]
c	Specific heat [$J \cdot kg^{-1} \cdot K^{-1}$]
CFD	Computational fluid dynamic
d	number of acquired data [-]
e	experimental detected value [°C or W]
$\dot{E}$	Energy per time unit per unit area [$W \cdot m^{-2}$]

EVA	Ethylene-vinyl acetate
F	View factor [-]
g	Gravity acceleration [$m \cdot s^{-2}$]
G	Solar radiation component [$W \cdot m^{-2}$]
Gr	Grashof number [-]
h	Heat transfer Coefficient [$W \cdot m^{-2} \cdot K^{-1}$]
i	Incidence angle [rad]
k	Thermal conductivity [$W \cdot m^{-1} \cdot K^{-1}$]
K	Correction factor of the optical properties [-]
l	Characteristic dimension [m]
L	Latitude [rad]
m	Mass [kg]
$\dot{m}$	Flow rate [kg/s]
$\overline{M}$	Mean value of the acquired experimental data [°C or W]
MBE	Mean bias error [°C or W]
NSE	Nash-Sutcliffe coefficient [%]
NOCT	Nominal Operating Cell Temperature [°C]
Nu	Nusselt number [-]
P	Perimeter [m]
Pr	Prandtl number [-]
p	Time step
PV	Photovoltaic module
q	Thermal flux [$W \cdot m^{-2}$]
$\dot{Q}$	Internal heat generation [$W \cdot m^{-3}$]
R	Solar radiation absorbed by the PV cell [$W \cdot m^{-2}$]
Ra	Rayleigh number [-]
Re	Reynolds number [-]
RMSE	Root mean square error [°C or W]
RMSEP	Root mean square error percentage [%]
v	Velocity [$m \cdot s^{-1}$]

Subscripts

air	external air
b	beam
ch	characteristic
conv	convective
d	diffuse
eff	effective
for	forced
g	generated
gl	glass
in	entering
m	position along the x direction
n	normal
nat	natural
out	leaving
pan	panel
PV	photovoltaic
r	reflected
rad	radiative
ref	reference
st	stored
surf	surface
ted	tedlar
w	water

Greek letters

α	Absorption coefficient [-]
β	Volumetric coefficient of thermal expansion [K^{-1}]
γ	Module azimuth [rad]

δ	Solar declination angle [rad]
ε	Emissivity [-]
ζ	Volumetric coefficient of thermal expansion [K^{-1}]
θ	Module inclination angle [rad]
ξ	PV cells temperature coefficient [K^{-1}]
ν	Cinematic viscosity [$m^2 \cdot s^{-1}$]
φ	Infrared thermal exchange with the sky [$W \cdot m^{-2}$]
ω	Solar hour angle [rad]
ρ	Density [$kg \cdot m^{-3}$]
σ	Stefan-Boltzmann constant [$W \cdot m^{-2} \cdot K^{-4}$]
τ	Transmission coefficient [-]
φ	Long wave thermal radiation from the sky [$W \cdot m^{-2}$]

1. Introduction

Solar energy is currently one of the major elements for a paradigm shift toward a more sustainable carbon-free energy scenario. Different technologies have been investigated to be able to produce energy on a larger scale [1–6], also considering the combination of different systems [7–9]. Solar photovoltaic is, in particular, one of the most promising and currently diffused technologies [10–13], that is playing a fundamental role in the transition toward a decarbonized society [14], with massive employment at the building level [15–19]. One of the main limitations is that only a small percentage of the incident solar radiation is transformed into electricity, whereas the remaining part is dissipated into heat, with an increase of the cell operating temperature that consequently leads to a decay of conversion efficiency. The increase in thermal efficiency is a topic widely discussed in the literature [20,21]. In an attempt to mitigate cell temperature and enhance PV performances, different types of cooling systems have been proposed and tested to improve the performances of traditional photovoltaic panels [22–24], including PVT systems [25] and the use of fans and artificial intelligence [26,27].

A viable and interesting solution appears the use of water-based systems [28,29]. Different configurations have been proposed and investigated where water can flow on the front glass or back surface or through pipes and channels realizing a PV/T configuration [23]. Also, water immersion of photovoltaic panels was studied as a cooling technique to improve panel performance [24,30].

Among these cooling techniques, a promising strategy to increase electrical efficiency is spray cooling on the PV back surface [31,32]. In this field, most of the research is based on experimental approaches, whereas the lack of appropriate theoretical models has to be noticed.

For instance, water-cooling sprinkler systems underneath polycrystalline photovoltaic modules have been tested [33] with continuous and intermittent cooling in the hottest hours of the day. Other experiments aiming to evaluate the PV cooling considering different irrigation strategies, water flow rates, and operating cycles were performed in a warm tropical climate in [34], however, these techniques were applied on the front surface with a natural worsening of the optical properties. Similarly, a water cooling system acting on the glass surface was installed on a large-scale 20 kW PV solar plant seeking to minimize the operation cost and the amount of water used as described in [35].

The impact of the cooling systems on the operative temperature, in relation to external meteorological conditions, is essential for estimating the actual performance of photovoltaic modules. Nevertheless, different methods for estimating the cell temperature, ranging from simple empirical correlations to more structured thermal and electrical models, are prevalently available for traditional PV panels without cooling systems. A simulation model based on finite differences that describe a double-glass multi-crystalline photovoltaic module was developed and validated using experimental data in [36]. A transient model to estimate the PV panels temperature, under time-varying field conditions, was proposed and validated in [37], successively a parametric study allowed to evaluate the effect of grid parameters on the model accuracy finding that smaller time steps produce lower RMSE despite an increment in the computational time. The same authors also proposed bidimensional transient numerical thermal models based on the finite difference method (FDM) developed in MATLAB environment, considering both explicit and implicit time schemes [38]. Among these models, the authors found that the explicit method is the most accurate but with greater computational effort. A three-dimensional CFD model was developed in Fluent to accurately simulate the airflow and the consequent thermal processes on the PV glass and the backsheet surface. Indeed, the convective heat transfer coefficients obtained from the numerical CFD simulation have been applied in a steady thermal model [39]. A mathematical approach developed to simultaneously solve a thermal and an electrical model was developed in [40] to determine the PV performance in transient conditions. However, the implemented 5-parameter electrical model introduced an additional complexity deriving from the need to obtain the electrical parameters, usually determined in the standard test conditions, for any operating condition.

Few works can be found in the literature that include thermal modeling of cooling systems. For instance, a computational CFD model was implemented in [41] to investigate the convective cooling mechanism on the PV backside.

A numerical 3-D model developed for a PV/T system equipped with different configurations of parallel channels on the PV module backside was proposed in [42] where the flow turbulence was simulated with the standard k–ε model. Another mathematical model was developed in [43] to determine the optimal control strategy to decide the activation of a PV cooling system according to the maximum allowable temperature, assuming steady-state conditions. Mainly, this validated model determines the cooling period length to attain a pre-set temperature drop. However, such an approach does not seem suitable to properly account for spray cooling in dynamic conditions. Specifically for the spray cooling technique, the increment of performance was evaluated by experimental campaigns both on the front and back sides of a small PV panel as described in [44]. The authors proposed to model the heat loss due to evaporation as a function of the difference between vapor partial pressures, of an evaporation factor depending on the water spray temperature and the conditions of the surrounding air, but then only experimental results were presented in the study. A pulsed-spray water cooling system for photovoltaic panels was proposed in [45], where a row of water jets was sprayed on the front side of the PV panel. The authors proposed a formulation where the heat lost by evaporation could be related to an evaporation factor, the latent heat of evaporation, and the difference in partial pressures. But again, results referred only to the experimental analysis. Following a different approach, a PV panel was modeled according to the thermo-electrical analogies by an RC circuit equipped with electrical resistances, and capacitances [46]. The RC model also considers the cooling effect due to an intermittent irrigation regime by a water film on a PV panel. A mathematical model based on a five-layer schematization of the panel was developed and validated in [47] with and without a water flow acting on the front surface. In particular, the cooling effect was modeled with an additional water layer where the energy balance is written and solved considering the amount of heat absorbed by the flowing water and the evaporation heat transfer.

Even though the literature confirms that water cooling is a promising and efficient technique, there are no currently available models to predict the operating temperature and power productions of a PV panel during spray cooling in presence of cooling systems. Therefore this study proposes to fill this gap by developing a novel dynamic thermal model of a PV panel that includes the modeling of a spray cooling system working on the back surface of the panel. The 1-D model allows for obtaining the temperature profile across the vertical section and, consequently, the electric energy produced when a water spray technique by means of nozzles is applied on the back surface. The model was validated thanks to the data obtained in the summer of 2019 by an extended experimental campaign carried out on a set-up installed at the University of Calabria (Italy). Furthermore, the numerical model allowed to analyze the cooling phenomena in detail to assess the importance of sensible and latent heat exchanges in the energy balance of the PV panel.

2. Methodology

The proposed thermophysical model is based on a previous work where a model for traditional PV panel was validated allowing to determine the temperature profile over the thickness, properly validated over different seasons [48]. The model refers to polycrystalline silicon (poly-Si) 245 W PV panel, tilted 30° on the horizontal surface. The panel was monitored to attain the experimental data required for validation (Fig. 1). The cells have a dimension of 156x156 mm, and the total dimension of the PV panel is 1663x998 mm. The module consists of the following layers: Glass, EVA top, PV cells, EVA bottom, and then Tedlar whose properties are reported in Table 1.

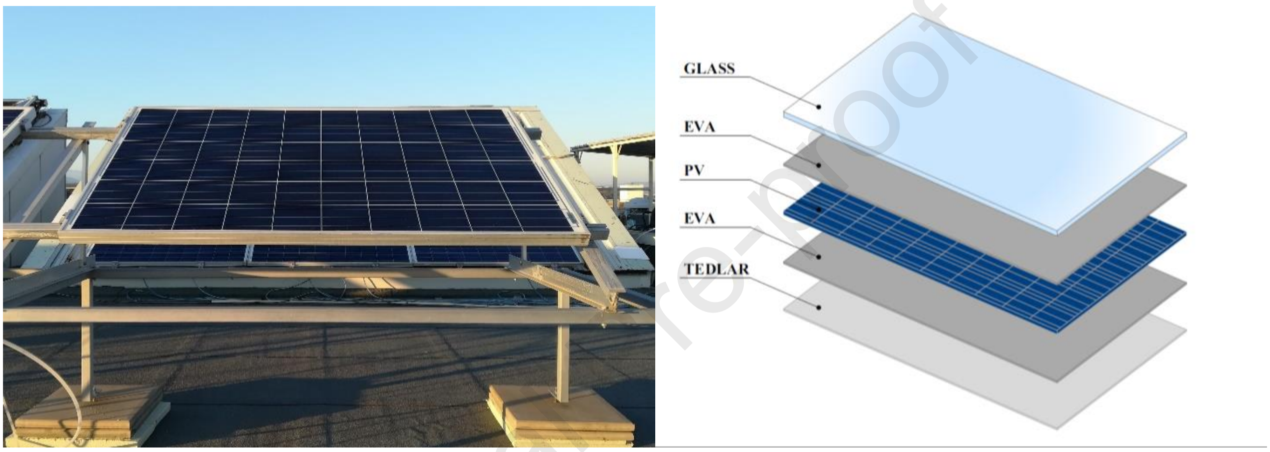

Fig. 1. PV module considered in the study (left) and schematic view of the main photovoltaic module layers (right)

Table 1. Thermal properties of the layers considered in the model [37]

Layer	**Thickness** (mm)	**Thermal conductivity k** ($W \cdot m^{-1} \cdot K^{-1}$)	**Density ρ** ($Kg \cdot m^{-3}$)	**Specific heat capacity c** ($J \cdot Kg^{-1} \cdot K^{-1}$)
Glass	3.2	1.8	3000	500
EVA top	0.2	0.35	960	2090
PV cells	0.3	148	2330	677
EVA bottom	0.2	0.35	960	2090
Tedlar	0.1	0.2	1200	1250

2.1. The experimental set-up

The experimental set-up is located on the roof of a building of the Department of Mechanical, Energy, and Management Engineering of the University of Calabria (Italy). It is made of different PV modules anchored on a structure with south orientation (Figure 3) and arranged to avoid mutual shading and be subjected to the same irradiance condition.

Fig. 2 Overview of the experimental site

The polycrystalline silicon modules have a total area of 1.46 m^2 and a nominal efficiency of 14.5 %. The electrical characteristics of the modules are reported in Table 2.

Table 2. Electric characteristics of the PV modules

Nominal power (W)	245
Output tolerance (W)	+5/-0
Rated voltage (V)	29.9
Rated current (A)	8.20
Open circuit voltage (V)	37.41
Short circuit current (A)	8.80
Temperature coefficient - P_{mpp} (%/°C)	-0.43
Temperature coefficient - I_{sc} (%/°C)	+0.06
Temperature coefficient - U_{oc} (%/°C)	-0.31
Normal Operating Cell Temperature (°C)	43±2

On the building roof, a weather station continuously monitors external meteorological climatic conditions, in particular: air temperature, relative humidity, wind speed and direction (but this last parameter is unused in the numerical model). The instrument characteristics are reported inTable 3.

Table 3. Sensors specification

	Temperature	**Relative humidity**	**Wind speed**

Sensor	Pt 100 1/3	Capacitive	Range	0…75 (m/s)
Range	-50…70 (°C)	0…100 (%)	Accuracy	2.5 %
Accuracy	0.1 (0 °C)	±1.5 (RH5-95%)	Threshold	0.5 (m/s)

The global solar irradiance on the module plane and the beam normal solar irradiance are measured with a Secondary Standard Eppley Laboratory where some pyranometers are arranged with a spectral range of 295-2800 nm, sensitivity of 8 μV/Wm^{-2}, a 95% response time of 5 s, a non-stability and non-linearity of 0.5 %, and uncertainty at an hourly average of 2%.

The experimental setup was built to perform experiments with different types of cooling systems that act on the back surface of the PV panels. The PV panel that is the object of the presented thermal model is equipped with two wide cone water spray nozzles installed at approximately 50 cm from the back surface in order to have a perpendicular spray that impacts cooling most of the rear surface (

Fig. 3). The nominal flow rate at a pressure of 3 bar is 8.55 l/min.

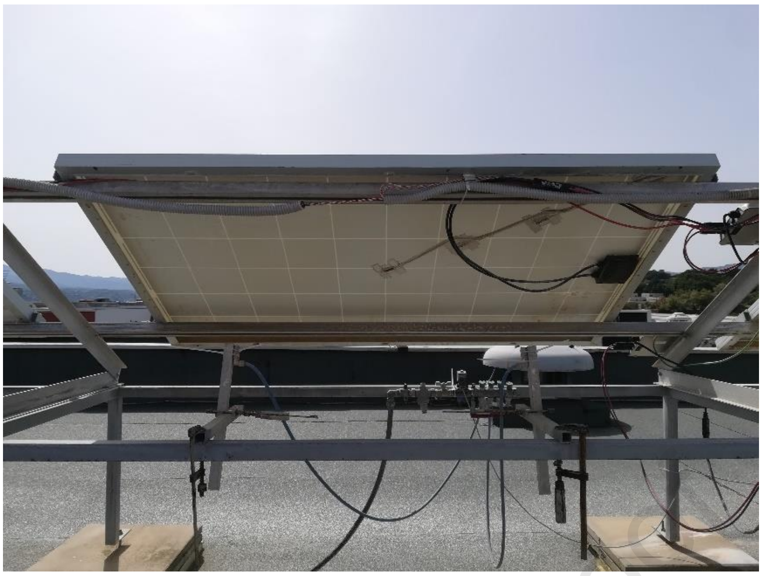

Fig. 3. PV panel equipped with spray cooling nozzles

On the back surface of the module, four temperature sensors are arranged in a diagonal direction from the center of the panel to the edge to verify temperature uniformity. The sensors are self-adhesive silicone rubber support with a thin film Pt100 Resistance Temperature Detector. The operative range is (-50; +150) °C with an accuracy of about 0.5 % of the measurement and a temperature coefficient lower than 0.02 %/°C. The sensors are installed to measure the radial distribution of the temperature, supposing a radial symmetry along the panel back surface. Starting from the outer position, close to the one edge of the panel, the sensor is named T_0 and successively the other three are placed radially to reach the module central position (T_3). From the experimental analysis, it was observed that the radial variations in temperature are very limited, in fact, in July the temperature varies on average by 0.755 ° C in the case of a cooled PV panel and by 0.241 ° C in the case of an uncooled PV panel. The major differences found in the case of a cooled PV panel are due to the imperfect uniformity of the spray which in the initial phase tends to cool more the surface in direct contact with the water jet. In the subsequent phases, the cooling phenomenon tends to become uniform. In the case of a cooled panel, the greatest radial temperature variations are maintained for limited time intervals. Therefore, what has been said justifies the hypothesis of a one-dimensional case in the modeling performed.

The cooling system is automatically activated by a solenoid valve controlled by the DAQ system. The valve activated when the temperature on the back surface reaches 40°C allowing the nozzle to spray water, and the duration of the spray was set to 5 s to be able to obtain experimental data coherent with the time step of the model. Indeed the spray cooling is a rather quick phenomenon that works on a very small time scale (the spray can last even less than one second) being therefore extremely difficult to model. In this particular case, the DAQ system did not allow, because of intrinsic limitation, to acquire data with a sample time lower than 5 s. Consequently, the period of the spray was set to 5 s to be coincident with the minimum possible time step allowed by the experimental measurements.

Furthermore, considering that to the aim of validation, the cardinal quantity is the back temperature of the PV module, this was acquired with a sample time of 5 s. All other variables, due to hardware limitation, were acquired with a sampling of 1 min, but to provide consistency with data used as input of the model, a linearization was performed obtaining interpolated data every 5 s in order to properly distribute the experimental data on the model time steps. The monitoring campaign was conducted in the summer months of 2020 from July to October. There was a scarce availability of data in August since maintenance operations were conducted on the building roof causing the stop of the data acquisition system.

The latter also registers every activation of the spray nozzles, providing an output file that was used as input to the model so that the numerical simulation is coherent with the physical phenomenon.

2.2. Optical and radiative model

The solar radiation per unit surface that is absorbed from the PV cells is assumed to be given by [49]:

$$G_{eff} = (\tau\alpha)_n \times (k_b \times G_b + k_d \times G_d + k_r \times G_r) \tag{1}$$

where G_b, G_d and G_r are the beam, diffuse and reflected radiation on the PV surface and k_b, k_d and k_r are correction coefficients that account for the variation of the optical properties of the glass surface $(\tau\alpha)$ in the function of the directional aspects of the radiation components. The generic correction coefficient is defined as [49]:

$$\mathrm{k}_{\tau\alpha} = \frac{(\tau\alpha)}{(\tau\alpha)_\mathrm{n}} \tag{2}$$

where $(\tau\alpha)_n$ is the product of front glass transmission coefficient τ_{gl} and the Pv cell absorption coefficient α_{PV}, both evelauated for a normal incidence. The coefficient $\mathrm{k}_{\tau\alpha}$ is clacualted distinctly for the different components of the solar radiation [50] as:

$$k_b = 1 + b_0 \times \left(\frac{1}{\cos\theta_b} - 1\right) \tag{3}$$

$$k_d = 1 + b_0 \times \left(\frac{1}{\cos\theta_d} - 1\right) \tag{4}$$

$$k_r = 1 + b_0 \times \left(\frac{1}{\cos\theta_r} - 1\right) \tag{5}$$

where b_0 is a constant that assumes different values according to the type of collector, set equal to 0.10 as suggested for single glazed collectors [36], θ_d and θ_r are the incidence angle of diffuse and reflected radiation, that can be calculated in function of the panel tilt angle according to the following experimental relationships [49]:

$$\theta_d = 59{,}68 - 0{,}1388 \times \beta + 0{,}001497 \times \beta^2 \tag{6}$$

$$\theta_r = 90 - 0{,}5788 \times \beta + 0{,}002693 \times \beta^2 \tag{7}$$

whereas the incident angle of the beam component θ_b is determined analytically as [49]:

$$cos\,\theta_b = sin(L - \beta)\,sin\,\delta + cos(L - \beta)\,cos\,\delta\,cos\,\omega \tag{8}$$

where L is the site latitude angle, δ is the solar declination angle and ω is the hour angle.

2.3. Thermal model

The thermal model is based on the general heat equation; a partial differential equation that for the proposed 1-D model can be written as [51]:

$$\rho \cdot c\,\frac{\partial T(x,t)}{\partial t} = k\,\cdot \frac{\partial^2 T(x,t)}{\partial x^2} + \dot{Q}(t) \tag{9}$$

where ρ is the density, *c* is the specific heat capacity, *k* is the thermal conductivity of the material, T is the one-dimensional temperature field over time, $\dot{Q}(t)$ is the internal heat generation and *x* is the direction along with the thickness.

The internal heat generation is due to the solar radiation absorbed in the different PV layers. In particular, for the nodes belonging to the glass layer, the front glass absorbs a share equal to $\alpha_{gl} \cdot G_{PV} \cdot A_{PV}$ where α_{gl} is the front glass absorption coefficient, set constant to 0.05 [37] since it is scarcely dependent on the incident angle. Heat generation is expressed per volume unit, therefore it is calculated as [48]:

$$\dot{Q}_{gl} = \frac{\alpha_{gl} \cdot G \cdot A_{pan}}{V_{gl}} \tag{10}$$

where the subscript *pan* refers to the whole area of the PV panel (1.66 m^2) and V_{gl} is the volume of the front glass that, for the monitored module, is 0.0053 m^3. In the PV cells, the part of the absorbed solar radiation that is not converted into electricity $(1 - \eta_{PV})$ is completely dissipated in heat, representing an internal heat source that can be expressed, per volume unit, as [48]:

$$\dot{Q}_{PV} = \frac{\alpha_{PV} \cdot \tau_{gl} \cdot A_{PV} \cdot G \cdot (1 - \eta_{PV})}{V_{PV}} \tag{11}$$

where A_{PV} is the total area of the PV cells (1.47 m^2), $V_{PV,cell}$ is the total volume of the PV cells (0.000498 m^3), η_{PV} is the electrical efficiency of the PV panel, determined by the Evans equation [52]:

$$\eta_{PV} = \eta_{PV,ref} \cdot [1 - \xi_{ref} \cdot (T_{PV} - T_{ref})] \tag{12}$$

where $\eta_{PV,ref}$ is the reference electrical efficiency, provided by the manufacturer, equal to 0.1487, T_{ref} is the reference temperature (298.15 K) and ξ_{ref} is the temperature coefficient of the PV cells that, for poly-crystalline modules, can be set to 0.0043 K^{-1} [52].

On the first and last node of the panel (front and back surface of the PV module) the convective heat transfer is computed with Eq. (13) [53]:

$$q_{conv} = h_{conv} \, (T_{surf} - T_{air}) \tag{13}$$

The convective heat transfer coefficient h_{conv} account both for forced and natural convection. A detailed methodology for their calculation is provided in Appendix B. The thermal properties of air in the proximity of the panel surface are calculated according to the relations reported in Appendix C.

The radiative heat losses for the front and back surfaces are accounted by means of a linearized radiative heat transfer coefficient (h_{rad}) [37].

$$q_{rad} = h_{rad,surf-sink} \, (T_{PV} - T_{amb}) \tag{14}$$

where the subscript *sink* refers to the sky or the ground, respectively for the front and the back surface.

The ground temperature is assumed to be equal to the ambient temperature. If no data of infrared exchanges with the sky are available, the sky temperature can be obtained from experimental relationships in the literature [54]. In this study the Alnaser model [55] was employed since for the specific case proved to be the most accurate:

$$T_{sky} = 0.6 \cdot T_{air} \tag{15}$$

Greater details on the choice of the appropriate sky temperature are reported in Appendix D where a comparison between the different models is reported. To be noticed that sky temperature is essential data for the calculation of the linearized radiative heat transfer coefficient.

2.4. Spray cooling model

Spray cooling is a rather complex phenomenon to model mathematically. Some approaches in the literature considered the definition of a convective heat transfer coefficient for the spray, basically neglecting the latent heat exchange, or globally incorporating it in the heat transfer coefficient.

Most of the works that model cooling phenomena are based on the definition of a convective heat transfer coefficient obtained from ad hoc correlation of the Nusselt number often expresses as a function of a fictive Reynolds number. Oliphant et al. [56] proposed a convective heat transfer coefficient obtainable from the following relation for the Nusselt cooling number:

$$Nu_{cool} = 32{,}5 \times (Re^{*})^{0{,}51} \qquad 10 \leq Re^{*} \leq 1000 \tag{16}$$

where Re is calculated as:

$$Re = \frac{G \times D_{spray}}{\mu_w} \tag{17}$$

and D_{spray} is the target surface diameter. Rybicki and Mudawar [57] proposed the following expression for the Nusselt cooling number:

$$Nu_{cool} = 4{,}7 \times Re^{0{,}61} \times \mathrm{Pr}_w^{0{,}32} \tag{18}$$

where Pr_{water} is the water Prandtl number and Re is calculated as:

$$Re = \frac{G \times d_{32}}{\mu_w} \tag{19}$$

where d_{32} is the Sauter mean diameter.

In this work, a different approach was adopted. From experimental observation on the specific spray cooling set-up, it was observed the cooling effect due to spray extends for a longer time, compared to the simulation set timestep, and develops including two main phases:

1. When the nozzles activate, the dominant effect is the sensible cooling due to the impact of water on the PV module back surface;
2. When the nozzles stop, the film of water on the back surface determines a dominant latent heat exchange that causes the same water evaporation in different timesteps.

To determine both terms that contribute to the cooling of the panel, it is essential to estimate beforehand the water flow rate of the nozzles.

To provide coherence between the simulated and experimental values, the time step of the model was set to 5 s, equalling the minimum allowable sample time of the DAQ system. Furthermore, the duration of each spray was also set to 5 s so that when the spray activates, it covers the entire duration of the time step.

From the Bernoulli equation, considering an incompressible fluid, neglecting water velocity at the inlet, and assuming no difference of height between the nozzle inlet and outlet it is possible to obtain the spray outlet velocity u_{out} that allows the calculation of the total outlet mass flow rate, and consequently the mass of water for each spray:

$$m_{cool} = \dot{m}_{nozzle} * \Delta t_{spray} = n_{nozzle} * \rho_{wat} * u_{out} * A_{out} * \Delta t_{spray} \tag{20}$$

where n_{nozzle} is the total number of employed nozzles, Δt_{spray} is the time duration of the spray, A_{out} is the nozzle outlet area and ρ_{wat} accounts for temperature variation and it is calculated according to the procedure reported in Appendix B.

A fraction of such mass does not reach the module back surface since:

- the spray cone is bigger than the PV back surface and some drops are lost;
- evaporation of a part of the spray occurs before reaching the PV surface;
- the bounce-back of some water particles that hit the surface.

So, it is possible to assume that at the end of the spray cycle (5 s) the effective mass deposited on the PV back surface is:

$$m_{cool,eff} = m_{cool} * \left(1 - \frac{PD}{100}\right) \tag{21}$$

where PD is the percentage of the mass of water that does not reach the surface because of the abovementioned aspects. Such quantity is left as a calibration parameter to set in order to improve the accuracy of the model. Finally, the spray effective mass flow rate per unit area that determines a cooling effect can be obtained as:

$$\dot{m}_{cool,eff} = \frac{m_{cool,eff}}{A_{PV} \times \Delta t_{spray}} \tag{22}$$

This mass produces a cooling effect that is attributed to the successive timestep. To consider the evaporation and the drop of a part of the water film on the module back surface in the subsequent iterations, a water mass balance is computed as:

$$m_{cool,eff}^{p} = m_{cool,eff}^{p-1} - m_{evap}^{p-1} - m_{drop}^{p-1} \tag{23}$$

where m_{drop}^{p-1} is the amount of "dropped" water at the previous timestep that does not remain on the module surface, obtainable as:

$$m_{drop} = m_{cool} * \left(\frac{PD}{100}\right) \tag{24}$$

and m_{evap}^{p-1} is the mass evaporated at the previous timestep because of the latent thermal exchange. Such contribution is more difficult to estimate. There are in the literature several empirical formulations that allow for evaluating the evaporated water flowrate for undisturbed fluids in the function of the saturation pressure evaluated at the film temperature, of the vapor pressure of air at external conditions and air velocity [58]. The methodology employed in the proposed model provides the evaporation mass flow rate per unit area as:

$$\dot{m}_{evap}^{p-1} = \frac{\left(0{,}089 + 0{,}0782 \times u_a^{p-1}\right) * (p_w^{p-1} - p_a^{p-1})}{\lambda^{p-1}} \tag{25}$$

where all the quantities are calculated at the previous timestep. The procedure for the evaluation of p_w, p_{sat}, and p_a are reported in Appendix E. Once such flow rate is calculated, the mass to be used in (23) can be simply obtained as:

$$m_{evap}^{p-1} = \dot{m}_{evap}^{p-1} * \Delta t_{cool} * A_{pan} \tag{26}$$

Finally, the sensible and latent contributions can be added together to determine the total cooling effect in the energy balance of the first node, determining the power extracted from the PV surface as:

$$\dot{E}_{cooling} = \dot{E}_{sens} + \dot{E}_{lat} = cp_{water} \times \dot{m}_{cool,eff} \times \left(T_m^{p+1} - T_{water}^{p+1}\right) + \lambda_{lat} \times \dot{m}_{evap} \tag{27}$$

where the term $\dot{m}_{evap}$ is once again evaluated with Eq. (25), but this time computed at the current time step *p*.

All the parameters used in the model are summarized in Table 4.

	Symbol	Description	Value
Weather data	I_{b0}	Horizontal beam solar radiation	Input file
	I_{d0}	Horizontal diffuse solar radiation	Input file
	T_{air}	Air temperature	Input file
Optical data	$(\tau\alpha)_n$	PV absorption × Glass Transmission coefficient	0.82
	α_{gl}	glass absorption coefficient	0.05
	ε_{surf}	PV Emission coefficient (front/back)	0.95/0.85
Solar data	β	PV tilt angle	30°
	L	Latitude angle	39.3°N
	H	hour of the day	1-24 h
	n	Progressive day number	1-365
Geometrical data	A_{pan}	Surface of the PV panel	1.66 m^2
	V_{gl}	Volume of the glass sheet	0.0053 m^3
	A_{PV}	Surface of the PV cells	1.47 m^2
	V_{PV}	Volume of the PV cells	$4.98 \cdot 10^{-4}$ m^3
Other data	$\eta_{PV,ref}$	Reference PV electric efficiency	14.87 %
	T_{water}	Water Temperature	Variable
	PD	Percentage of mass water that does not reach the back surface	For calibration

Table 4. Parameter used in the model

2.5. Energy balance method

The model is based on the energy balance method, performing for each timestep a balance between the energy entering, leaving, generating and accumulating into the considered volume [37].

$$\dot{E}_{in} + \dot{E}_{g} = \dot{E}_{st} + \dot{E}_{out} \tag{28}$$

where $\dot{E}_{in}$ is the energy entering the control volume, $\dot{E}_{out}$ is the energy leaving the control volume, $\dot{E}_{g}$ is the heat generated into the volume and $\dot{E}_{st}$ is the energy stored in the control volume.

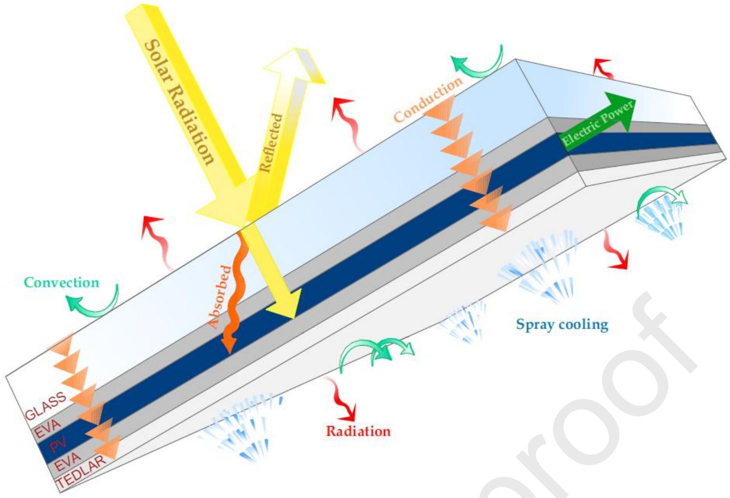

Fig. 4. Schematic representation of the nodes heat balances

Applying the Finite Difference (FD) method, the general heat equation is approximated with an algebraic equation, choosing for the model an implicit time scheme so that the spatial derivatives of the heat equation are solved at the future time (*p+1*). The PV panel was discretized in 161 nodes along with its thickness. The number of nodes was initially chosen in order to have the possibility to properly represent all the layers of a PV panel. Some of these layers (such as Tedlar and EVA) have such a small thickness that it is necessary to define a very small Δx to keep them into account. This was the main criterion in defining the minimum number of elements. Furthermore, a series of preliminary simulations allowed to see that a further increase in the number of nodes, did not produce noticeable variation in results.

The equations cannot be solved directly and after writing the energy balance for each node, a system of *n* algebraic equations is obtained, where the nodal temperatures are the unknown quantities at each time step.

In the following, some equations referring to the most representative nodes are reported. It must be noted that all energy exchanges are assumed to be positive, therefore there are no terms relating to energy leaving the node.

For the *top surface node*:

$$\dot{\mathbf{E}}_{\mathbf{in}} = \mathrm{k_{gl}} \cdot \left(\frac{\mathrm{T_{m-1}^{p+1}} - \mathrm{T_{m}^{p+1}}}{\Delta \mathrm{x}}\right) + \mathrm{h_{conv}} \cdot \left(\mathrm{T_{air}} - \mathrm{T_{m}^{p+1}}\right) + \mathrm{h_{rad,gl-sky}} \cdot \left(\mathrm{T_{sky}} - \mathrm{T_{m}^{p+1}}\right) + \mathrm{h_{rad,gl-ground}} \cdot \left(\mathrm{T_{ground}} - \mathrm{T_{m}^{p+1}}\right) \quad (29)$$

$$\dot{\mathbf{E}}_{\mathbf{g}} = \dot{Q}_{gl} \cdot \frac{\Delta x}{2}$$

$$\dot{\mathbf{E}}_{\mathbf{st}} = \left(\rho_{gl} \cdot c_{gl} \cdot \frac{\Delta x}{2}\right) \cdot \left(\frac{T_m^{p+1} - T_m^p}{\Delta t}\right)$$

and rearranging the terms:

$$T_m^{p+1} \cdot \left(\frac{\rho_{gl} \cdot c_{gl} \cdot \Delta x}{2\Delta t} + \frac{k_{gl}}{\Delta x} + h_{conv} + h_{rad,gl-sky} + h_{rad,gl-ground}\right) - T_{m-1}^{p+1} \cdot \left(\frac{k_{gl}}{\Delta x}\right) = (T_{air} \cdot h_{conv} + T_{sky} \cdot h_{rad,gl-sky} + T_{ground} \cdot h_{rad,gl-ground} + \dot{Q}_{gl} \cdot \frac{\Delta x}{2}) + \left(\frac{\rho_{gl} \cdot c_{gl} \cdot \Delta x}{2\Delta t}\right) \cdot T_m^p \tag{30}$$

For interior PV nodes:

$$\dot{\boldsymbol{E}}_{\boldsymbol{in}} = k_{PV} \cdot \left(\frac{T_{m+1}^{p+1} - T_m^{p+1}}{\Delta x}\right) + k_{PV} \cdot \left(\frac{T_{m-1}^{p+1} - T_m^{p+1}}{\Delta x}\right)$$

$$\dot{\boldsymbol{E}}_{\boldsymbol{g}} = \dot{Q}_{PV} \cdot \Delta x \tag{31}$$

$$\dot{\boldsymbol{E}}_{\boldsymbol{stor}} = (\rho_{PV} \cdot c_{PV} \cdot \Delta x) \cdot \left(\frac{T_m^{p+1} - T_m^p}{\Delta t}\right)$$

and rearranging the terms:

$$-\left(\frac{k_{PV}}{\Delta x}\right) \cdot T_{m-1}^{p+1} + \left(2\frac{k_{PV}}{\Delta x} + \frac{\varrho_{PV} \cdot c_{PV} \cdot \Delta x}{\Delta t}\right) \cdot T_m^{p+1} - \left(\frac{k_{PV}}{\Delta x}\right) \cdot T_{m+1}^{p+1} = \left(\dot{Q}_{PV} \cdot \Delta x\right) + \left(\frac{\varrho_{PV} \cdot c_{PV} \cdot \Delta x}{\Delta t}\right) \cdot T_m^p \tag{32}$$

Different nodes are modeled as interfaces between two different materials. For instance, for the *EVA-Tedlar* node the energy contributions are:

$$\dot{\mathbf{E}}_{\mathbf{in}} = k_{EVA} \cdot \left(\frac{T_{m+1}^{p+1} - T_m^{p+1}}{\Delta x}\right) + k_{ted} \cdot \left(\frac{T_{m-1}^{p+1} - T_m^{p+1}}{\Delta x}\right)$$

$$\dot{\mathbf{E}}_{\mathbf{g}} = 0 \tag{33}$$

$$\dot{\mathbf{E}}_{\mathbf{st}} = \left(\rho_{EVA} \cdot c_{EVA} \cdot \frac{\Delta x}{2}\right) \cdot \left(\frac{T_m^{p+1} - T_m^p}{\Delta t}\right) + \left(\rho_{ted} \cdot c_{ted} \cdot \frac{\Delta x}{2}\right) \cdot \left(\frac{T_m^{p+1} - T_m^p}{\Delta t}\right)$$

and applying the energy balance and rearranging the terms it is possible to obtain:

$$-\left(\frac{k_{ted}}{\Delta x}\right)\cdot T_{m-1}^{p+1}+\left[\frac{k_{EVA}}{\Delta x}+\frac{k_{ted}}{\Delta x}+\frac{\Delta x}{2\,\Delta t}\cdot(\rho_{EVA}\cdot c_{EVA}+\rho_{ted}\cdot c_{ted})\right]\cdot T_m^{p+1}-\left(\frac{k_{EVA}}{\Delta x}\right)\cdot T_{m+1}^{p+1}=\left(\frac{\Delta x}{2\Delta t}\right)\cdot(\rho_{EVA}\cdot c_{EVA}+\rho_{ted}\cdot c_{ted})\cdot T_m^p \quad (34)$$

the EVA-PV cell interface node has the following terms:

$$\dot{\boldsymbol{E}}_{\boldsymbol{in}}=k_{PV}\cdot\left(\frac{T_{m+1}^{p+1}-T_m^{p+1}}{\Delta x}\right)+k_{EVA}\cdot\left(\frac{T_{m-1}^{p+1}-T_m^{p+1}}{\Delta x}\right)$$

$$\dot{\boldsymbol{E}}_{\boldsymbol{g}}=\dot{Q}_{PV}\cdot\frac{\Delta x}{2} \quad (35)$$

$$\dot{\boldsymbol{E}}_{\boldsymbol{stor}}=\left(\rho_{PV}\cdot c_{PV}\cdot\frac{\Delta x}{2}\right)\cdot\left(\frac{T_m^{p+1}-T_m^p}{\Delta t}\right)\left(\rho_{EVA}\cdot c_{EVA}\cdot\frac{\Delta x}{2}\right)\cdot\left(\frac{T_m^{p+1}-T_m^p}{\Delta t}\right)$$

and applying the energy balance and rearranging the terms it is possible to obtain:

$$-\left(\frac{k_{EVA}}{\Delta x}\right)\cdot T_{m-1}^{p+1}+\left[\frac{\Delta x}{2\times\Delta t}\cdot(\rho_{EVA}\cdot c_{EVA}+\rho_{PV}\cdot c_{PV})+\frac{k_{PV}}{\Delta x}+\frac{k_{EVA}}{\Delta x}\right]\cdot T_m^{p+1}-\left(\frac{k_{PV}}{\Delta x}\right)\cdot T_{m+1}^{p+1}=\frac{\Delta x}{2\times\Delta t}\cdot(\rho_{EVA}\cdot c_{EVA}+\rho_{PV}\cdot c_{PV})\cdot T_m^p+\dot{Q}_{PV}\cdot\frac{\Delta x}{2} \quad (36)$$

Finally, and more importantly, the energy balance of the bottom node (back surface of the PV panel), accounts for the cooling contribution due to water spray (Eq. (27)) and is made of the following terms:

$$\begin{aligned}\dot{\mathbf{E}}_{\mathbf{in}}=\;&k_{ted}\cdot\left(\frac{T_{m+1}^{p+1}-T_m^{p+1}}{\Delta x}\right)+h_{conv}\cdot\left(T_{amb}-T_m^{p+1}\right)+h_{rad,ted-sky}\cdot\left(T_{sky}-T_m^{p+1}\right)\\&+h_{rad,gl-ground}\cdot\left(T_{ground}-T_m^{p+1}\right)-\left(cp_w\cdot G_{film}\cdot\left(T_m^{p+1}-T_w^{p+1}\right)\right.\\&\left.+\lambda_{lat}\cdot\dot{m}_{evap}\right)\end{aligned} \quad (37)$$

$$\dot{\mathbf{E}}_{\mathbf{g}}=0$$

$$\dot{\mathbf{E}}_{\mathbf{st}}=\left(\rho_{ted}\cdot c_{ted}\cdot\frac{\Delta x}{2}\right)\left(\frac{T_m^{p+1}-T_m^p}{\Delta t}\right)$$

Applying the energy balance and rearranging the terms it is possible to obtain:

$$\left(\frac{k_{ted}}{\Delta x}+h_{conv}+h_{rad,ted-sky}+h_{rad,ted-grd}+\frac{\rho_{ted}\cdot c_{ted}\cdot\Delta x}{2\cdot\Delta t}+cp_w\cdot G_{film}\right)\cdot T_m^{p+1}-\left(\frac{k_{ted}}{\Delta x}\right)\cdot T_{m+1}^{p+1}=\left(h_{conv}\cdot T_{amb}+h_{rad,ted-sky}\cdot T_{sky}+h_{rad,ted-grd}\cdot T_{grd}+cp_w\cdot G_{film}\cdot T_w^{p+1}-\lambda_{lat}\cdot\dot{m}_{evap}\right)+\left(\frac{\rho_{ted}\cdot c_{ted}\cdot\Delta x}{2\cdot\Delta t}\right)\cdot T_m^p \quad (38)$$

After writing the energy balances for all nodes of the domain a system of linear equations is obtained. The nodal equations are arranged in matrix form as follows:

$$[A]\{T\} = \{B\} \tag{39}$$

where [A] is a $n \times n$ tridiagonal square matrix of lumped terms multiplying the nodal temperatures, {T} is the unknown nodal temperatures $n \times 1$ vector and {B} is a $n \times 1$ vector of known terms not associated with any variable.

$$\begin{bmatrix} A_{1,1} & A_{1,2} & \cdots & A_{1,n-1} & A_{1,n} \\ A_{2,1} & A_{2,2} & & A_{2,n-1} & A_{2,n} \\ \vdots & & \ddots & \vdots & \\ A_{n-1,1} & A_{n-1,2} & \cdots & A_{n-1,n-1} & A_{n-1,n} \\ A_{n,1} & A_{n,2} & & A_{n,n-1} & A_{nn} \end{bmatrix} \begin{Bmatrix} T_1^{p+1} \\ T_2^{p+1} \\ \vdots \\ T_{n-1}^{p+1} \\ T_n^{p+1} \end{Bmatrix} = \begin{Bmatrix} B_1 \\ B_2 \\ \vdots \\ \vdots \\ B_{n-1} \\ B_n \end{Bmatrix} \tag{40}$$

The thermal model was then implemented as a numerical code trhough Python language, where external experimental data for boundary conditions were imported and the unknown nodal temperature vector was solved for each time step.

2.6. Uncertainty analysis

The numerical model developed requires as input data some climatic and meteorological quantities. In particular, it must be provided the external air temperature and relative humidity, the wind speed, the intensity of the direct solar radiation incident on the normal plane, and the intensity of the global solar radiation on the tilted plane. These quantities are measured by means of different instruments installed in the experimental site. Each instrument has a different accuracy and generates errors in the measurements that affect the goodness of the final results [27]. In order to evaluate the influence of the errors of the individual measured quantities on the final results, the *theory of uncertainty propagation* (or *error propagation*) is applied. This methodology allows for evaluating the effects of the uncertainty of the independent variables x_i on the property R based on them. The procedure to calculate the propagation of the error is proposed by Kline and McClintock [59]. Considering a generic quantity:

$$R = R(x_1 + x_2 + \cdots + x_n) \tag{41}$$

where the x_i are the independent variables, it is possible to determine the global uncertainty by means of:

$$\omega_R = \frac{\partial R}{\partial x_1}\omega_1 + \frac{\partial R}{\partial x_2}\omega_2 + \cdots + \frac{\partial R}{\partial x_n}\omega_n \tag{42}$$

where the ω_i are the uncertainties of the single measuring instruments. In the engineering field, by applying the theory of error propagation to simple functions, it is possible to apply the following formula to determine the global uncertainty:

$$\omega_R = \sqrt[2]{\sum_{i=1}^{n} (\omega_i)^2} \tag{43}$$

For the case in question, the uncertainties of the measuring instruments used are summarized in Table 5:

Table 5. Percentual accuracy of the sensors

Property	Percentage accuracy [%]
Air temperature	0,5
Air relative humidity	3
Wind velocity	2,5
Beam normal radiation	2
Global radiation on the tilted surface	2

Consequently, the global uncertainty for the examined case is equal to:

$$\omega_{GLOBAL} = \sqrt[2]{\omega_{T_{air}}^2 + \omega_{HR_{air}}^2 + \omega_{v_w}^2 + \omega_{I_{bn}}^2 + \omega_{G_{tilted}}^2} = 5{,}61\% \tag{44}$$

2.7. Validation indexes

The accuracy of the model was evaluated by comparing experimental data acquired over a long campaign of monitoring and simulated data from the model.

For a wider and strong validity assessment, different statistical indexes were considered:

- Root mean square error (**RMSE**), given by:

$$\mathbf{RMSE} = \sqrt{\frac{\sum_{i=1}^{d} (m_i - e_i)^2}{d}} \tag{45}$$

where *m* is the modelled value, *e* is the experimentally measured value and *d* is the number of data points. The lower the RMSE the greater is the accuracy of the model in predicting data.

- Root mean square error percentage (**RMSEP**), namely the root mean square error evaluated in percentage on the measured data. Such an index normalizes the error compared to the dimension of the considered parameter.

$$\mathbf{RMSEP} = \sqrt{\frac{\sum_{i=1}^{d}\left(\frac{m_i - e_i}{e_i}\right)^2}{d}} \tag{46}$$

- Mean bias error (**MBE**), given by:

$$\mathbf{MBE} = \frac{\sum_{\mathrm{i=1}}^{\mathrm{d}}(\mathrm{m_i} - \mathrm{e_i})}{\mathrm{d}\sum_{\mathrm{i=1}}^{\mathrm{d}}(\mathrm{e_i})} \tag{47}$$

through which it is possible to understand whether the model provides an overestimation (positive sign) or an underestimation (negative sign) of the data predicted.

- Nash-Sutcliffe coefficient (**NSE**), given by:

$$\mathbf{NSE} = 1 - \frac{\sum_{\mathrm{i=1}}^{\mathrm{d}}(\mathrm{m_i} - \mathrm{e_i})^2}{\sum_{\mathrm{i=1}}^{\mathrm{d}}(\mathrm{e_i} - \overline{\mathrm{M}})^2} \tag{48}$$

Where $\overline{\mathrm{M}}$ is the average value of the observed data. The NSE value can vary from -∞ to 1: a value of 1 (NSE = 1) indicates a perfect correspondence between the modelled and observed data; a value equal to 0 (NSE = 0) instead indicates that the predictions of the model are accurate as the average of the observed values, while a value lower than zero (NSE <0) occurs in the case in which the observed average estimates the results better than the model, in other words, when the residual variance, represented by the numerator, is greater than the variance of the data, represented by the denominator. The predictions of the model can be considered sufficiently accurate when the NSE index is greater than 0.75.

3. Results and discussion

3.1. Validation of the model

Simulations with the developed model were performed for all the available days in the period of the experimental campaign. To validate the model, the results of the simulations were compared with the PV back surface temperature and output electrical power. Results of the comparison are reported in Fig. 5 and Fig. 6, where some representative days were selected in July, September and October to show the accuracy of the model in predicting temperature and electrical power. The trends of climatic and meteorological quantities for the days examined are reported in Appendix E.

The figures show the good agreement between experimental and simulated data. The model can accurately follow the trend of electrical power whereas a slightly lower accuracy is found for the temperature. In particular, the model intends to show smaller oscillations when the cooling system activates (at an average temperature of 40 °C on the back surface) whereas the system actually produces greater temperature drops. It has to be considered that on the experimental module back surface four temperatures are measured, and because of the bidimensional effect, a gradient on the surface can be appreciated. The thermal model, being mono-dimensional, predicts a single temperature assuming an isothermal back surface. This can cause the difference detected between experimental and simulated data. Nevertheless, considering the overall trend, the accuracy is fairly good.

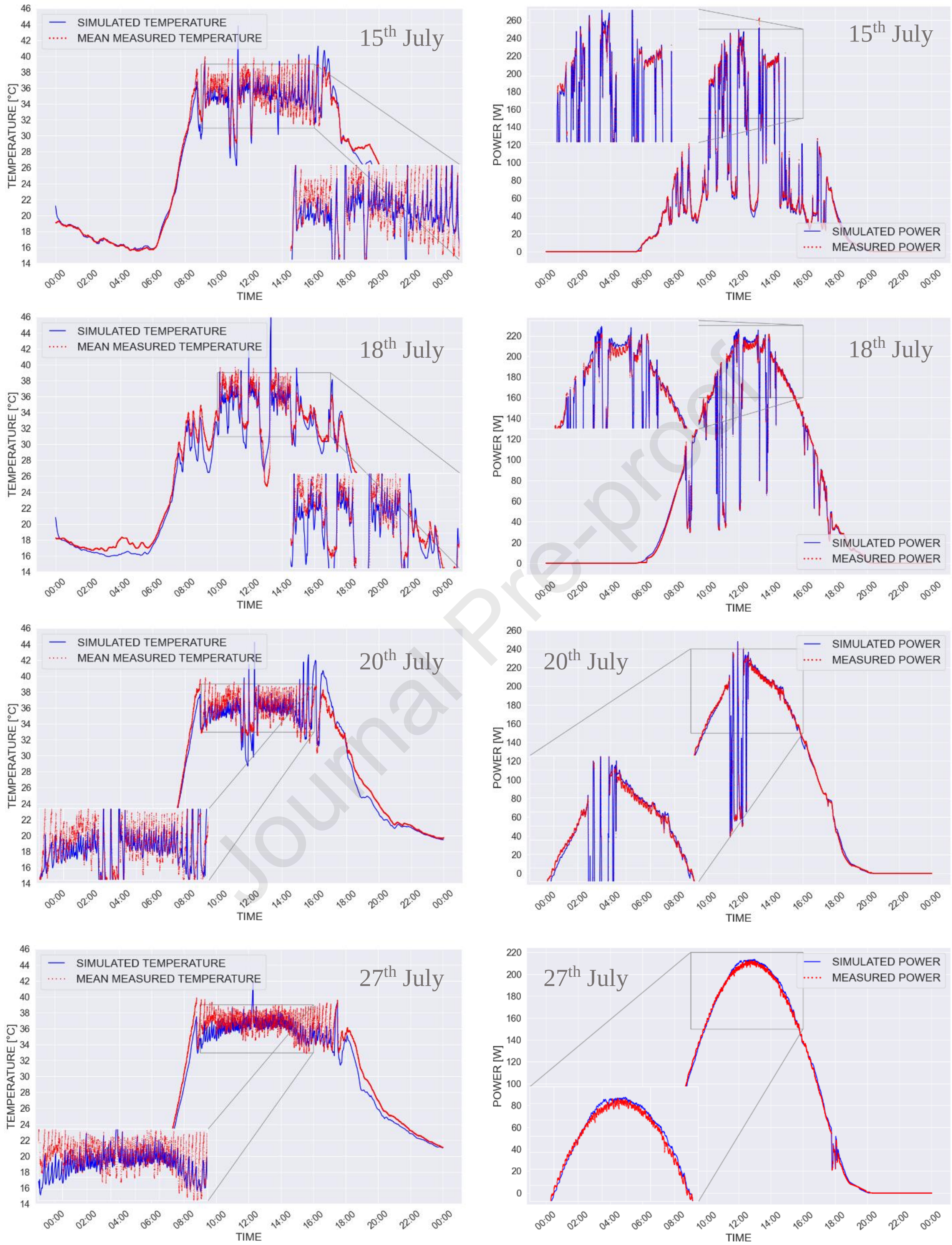

Fig. 5. Simulated and experimental trends of temperature and electrical power for selected days in July

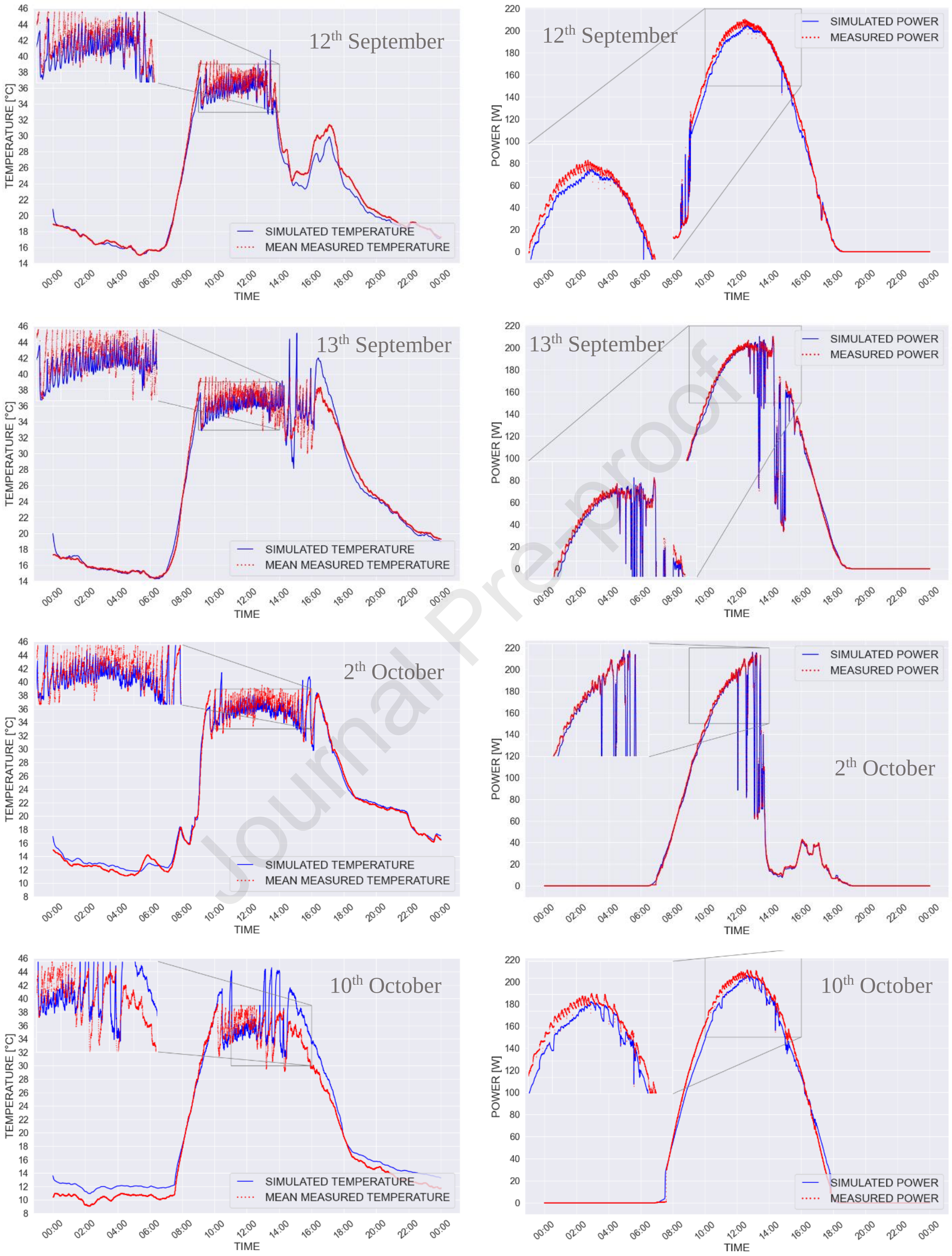

Fig. 6. Simulated and experimental trends of temperature and electrical power for selected days in September and October

Table 6. Daily correlation indexed for temperature and output electric power in the period of the experimental campaign

	TEMPERATURE			**POWER**				**TEMPERATURE**			**POWER**				**TEMPERATURE**			**POWER**		
DATE	**RMSE**	**RMSEP**	**NSE**	**RMSE**	**RMSEP**	**NSE**	DATE	**RMSE**	**RMSEP**	**NSE**	**RMSE**	**RMSEP**	**NSE**	DATE	**RMSE**	**RMSEP**	**NSE**	**RMSE**	**RMSEP**	**NSE**
15/7/2020	1.30	0.0042	0.9730	2.66	0.3309	0.9988	**12/9/2020**	1.07	0.0035	0.9811	1.76	0.2870	0.9993	**05/10/2021**	1.33	0.0044	0.9573	2.93	0.2216	0.9955
16/7/2020	1.29	0.0042	0.9712	2.38	0.3181	0.9991	**13/9/2020**	1.26	0.0041	0.9801	2.30	0.4654	0.9991	**06/10/2021**	1.50	0.0049	0.9532	3.94	0.3502	0.9970
17/7/2020	1.34	0.0044	0.9710	2.53	0.3957	0.9988	**14/9/2020**	1.07	0.0035	0.9836	2.13	0.4604	0.9992	**07/10/2021**	1.01	0.0034	0.9081	1.73	0.3698	0.9915
18/7/2020	1.39	0.0046	0.9669	2.79	0.3084	0.9982	**15/9/2020**	1.31	0.0043	0.9643	1.87	0.3388	0.9982	**08/10/2021**	1.53	0.0051	0.9752	6.23	0.3539	0.9934
19/7/2020	1.43	0.0047	0.9715	3.04	0.2820	0.9982	**16/9/2020**	1.31	0.0043	0.9738	2.17	0.3279	0.9984	**09/10/2021**	2.22	0.0074	0.9652	5.44	0.3741	0.9955
20/7/2020	1.17	0.0038	0.9821	4.29	0.5258	0.9971	**17/9/2020**	1.17	0.0039	0.9533	2.73	0.3687	0.9932	**11/10/2021**	1.89	0.0063	0.9665	5.23	0.3001	0.9956
21/7/2020	1.24	0.0040	0.9757	2.22	0.3684	0.9993	**18/9/2020**	1.22	0.0040	0.9756	3.03	0.3783	0.9984	**12/10/2021**	0.75	0.0026	0.8797	1.50	0.6213	0.9834
22/7/2020	1.33	0.0043	0.9717	2.51	0.3888	0.9990	**19/9/2020**	1.08	0.0035	0.9851	3.02	0.2479	0.9985	**13/10/2021**	1.27	0.0043	0.9755	4.42	0.4154	0.9953
23/7/2020	1.33	0.0043	0.9640	2.10	0.3276	0.9993	**20/9/2020**	1.28	0.0041	0.9760	2.92	0.2672	0.9985	**14/10/2021**	0.90	0.0031	0.9740	2.35	0.2166	0.9942
24/7/2020	1.49	0.0048	0.9540	2.18	0.3381	0.9992	**21/9/2020**	1.33	0.0043	0.9700	3.03	0.3277	0.9984	**15/10/2021**	1.82	0.0061	0.8990	4.45	0.3514	0.9887
25/7/2020	1.48	0.0048	0.9598	2.04	0.3457	0.9993	**22/9/2020**	1.34	0.0044	0.9630	2.94	0.2730	0.9975	**16/10/2021**	1.27	0.0042	0.9764	5.48	0.3262	0.9940
26/7/2020	1.62	0.0053	0.9525	4.07	0.4293	0.9973	**23/9/2020**	1.17	0.0038	0.9647	2.81	0.2950	0.9980	**19/10/2021**	1.42	0.0048	0.9852	4.18	0.1908	0.9976
27/7/2020	1.24	0.0040	0.9739	2.21	0.3621	0.9993	**24/9/2020**	1.17	0.0038	0.9786	4.66	0.4268	0.9963	**20/10/2021**	1.63	0.0056	0.9837	5.79	0.3126	0.9945
28/7/2020	1.13	0.0037	0.9788	2.38	0.3928	0.9991	**25/9/2020**	1.22	0.0040	0.9710	3.23	0.4141	0.9984	**21/10/2021**	1.80	0.0062	0.9814	6.63	0.3469	0.9929
29/7/2020	1.30	0.0042	0.9654	2.02	0.3601	0.9993	**27/9/2020**	1.37	0.0045	0.9681	4.10	0.2374	0.9959	**22/10/2021**	2.13	0.0073	0.9739	5.54	0.5858	0.9951
30/7/2020	1.38	0.0045	0.9604	1.92	0.3015	0.9994	**28/9/2020**	1.63	0.0055	0.9220	4.69	0.4876	0.9922	**25/10/2021**	1.13	0.0038	0.9739	3.87	0.3374	0.9930
31/7/2020	1.38	0.0045	0.9513	1.70	0.4083	0.9992	**29/9/2020**	1.65	0.0054	0.9670	4.86	0.3338	0.9966	**26/10/2021**	2.03	0.0068	0.9494	4.70	0.2594	0.9940
01/8/2020	1.42	0.0046	0.9434	3.22	0.3410	0.9981	**01/10/2021**	1.77	0.0058	0.9705	4.33	0.3221	0.9971	**27/10/2021**	1.50	0.0052	0.9636	4.25	0.4602	0.9883
02/8/2020	1.42	0.0046	0.9544	1.99	0.3067	0.9994	**02/10/2021**	0.95	0.0031	0.9909	3.90	0.6617	0.9976	**28/10/2021**	1.13	0.0038	0.9517	1.97	0.3938	0.9938
10/9/2020	1.09	0.0035	0.9825	2.00	0.4144	0.9994	**03/10/2021**	1.26	0.0041	0.9783	3.39	0.2970	0.9959	**29/10/2021**	1.47	0.0049	0.9777	6.43	0.3590	0.9925
11/9/2020	1.26	0.0041	0.9744	1.98	0.4677	0.9993	**04/10/2021**	1.47	0.0048	0.9585	3.72	0.3075	0.9975	**30/10/2021**	1.71	0.0056	0.9741	6.50	0.2887	0.9903

Further confirmation of the accuracy of the model in predicting the working condition of the cooled PV panel appears from previous Table 6 which reports the daily correlation indexes evaluated for the whole period of the experimental campaign. The indexes are separately calculated for temperature and electric power. It can be appreciated how in the hot months of July and August, the RSME does not overcome the value of 1.62 °C. The correlation index NSE assumes always high values ranging from 0.934 to 0.9821 and therefore demonstrates a good correlation between experimental and predicted values. The mean square error in the case of electric power reaches a maximum of 4.3 W but the NSE assumed higher values, from 0.9971 to 0.9994, indicating an excellent correlation.

In September, the results for the temperature and power provided mean square errors and NSE values in the same range as July and August. In October slightly lower correlations were appreciated, with a maximum RMSE of 2.2 °C and NSE values in the range between 0.8797 and 0.9852. Again the predicted power showed a more accurate correlation with an NSE ranging from 0.9834 to 0.9976, even though a maximum RMSE of 6.63 W was observed.

3.2. Analysis of the cooling phenomena

To assess the effect of the spray cooling on the PV panel, a more detailed analysis was conducted to highlight the sensible and latent heat extracted from the panel back surface and compare it with the case of a traditional non-cooled panel. Fig. 7a shows the trends of radiative, convective, accumulated, and conduction thermal power for the traditional PV panel back surface node in one day of July. The trends of some climatic and meteorological quantities are reported in Appendix E for the examined day. As can be expected, in absence of cooling systems, the major term of the energy balance during the insolated hours of the day is due to the heat transferred from upper interior nodes by conduction, and once it reaches the back surface of the panel it is dissipated through convection and radiative exchanges with the sky and the surrounding ground. The conductive term reaches a maximum of around 400 W/m^2 in the central part of the day and displays a typical bell-shaped curve, symmetric to noon. The radiative heat transfer amounts at most to 150 W/m^2 (in absolute terms), whereas the convective term overcomes the 200 W/m^2 (in absolute terms). The heat accumulation into the node is, as expected, almost negligible. When the cooling system is added to the model, the sensible and latent heat exchange terms appear, strongly modifying the thermal balance of the back surface node (Fig. 7b).

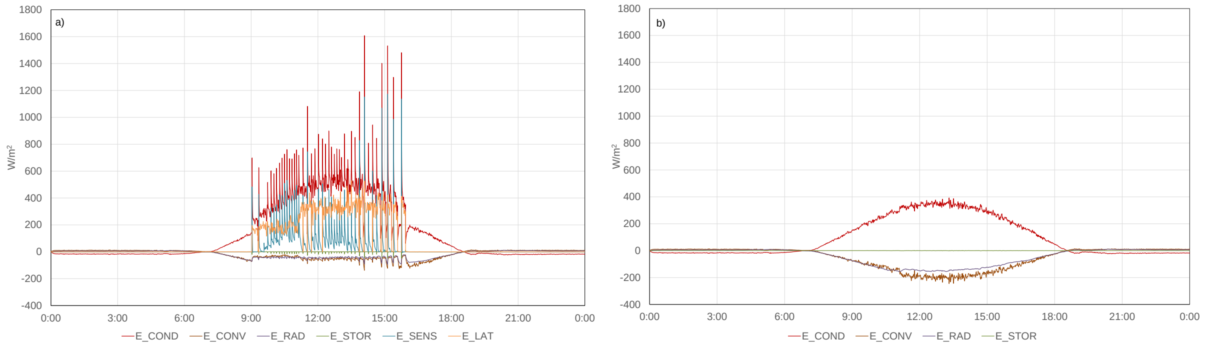

Fig. 7. Energy balance contributions on the first node of the panel (back surface) 16th of July. With cooling system a) and without cooling system b)

It clearly appears how both sensible and latent contributions play an important role in the node energy balance. After the sunrise, before reaching the temperature activation threshold, there is neither sensible nor latent contribution and the conductive heat coming from upper nodes is dissipated again through convection and radiation to the external environment, while the stored heat assumes a negligible value. Once the back surface temperature reaches 40 °C the spray cooling activates and the related energy terms appear in the balance. After the spray activation, the heat transferred from upper nodes is mainly dissipated by the water spray and consequently, convection and radiation assume more modest values.

Fig. 8 reports, in more detail, the energy contributions for the selected day of 16th of July at two different times of spray activation; in particular, the first activation of the day and the one with the highest heat extraction. At the time step in which the spray occurs the sensible heat transfer booms to a considerable high value, then gradually tends to zero in the following iterations. In the successive time step, the latent contribution appears providing also an important rate of heat transfer. Because of the temperature drop induced by the cooling of the back surface, a high temperature gradient between the last two nodes of the panel is established, and consequently, the conduction term assumes significant values, reaching 700 W/m^2 in the first case and 1532 W/m^2 in the second one. The sensible heat flux shows a peak of 483 W/m^2 after the first spray of the day and 1173 W/m^2 in the second case.

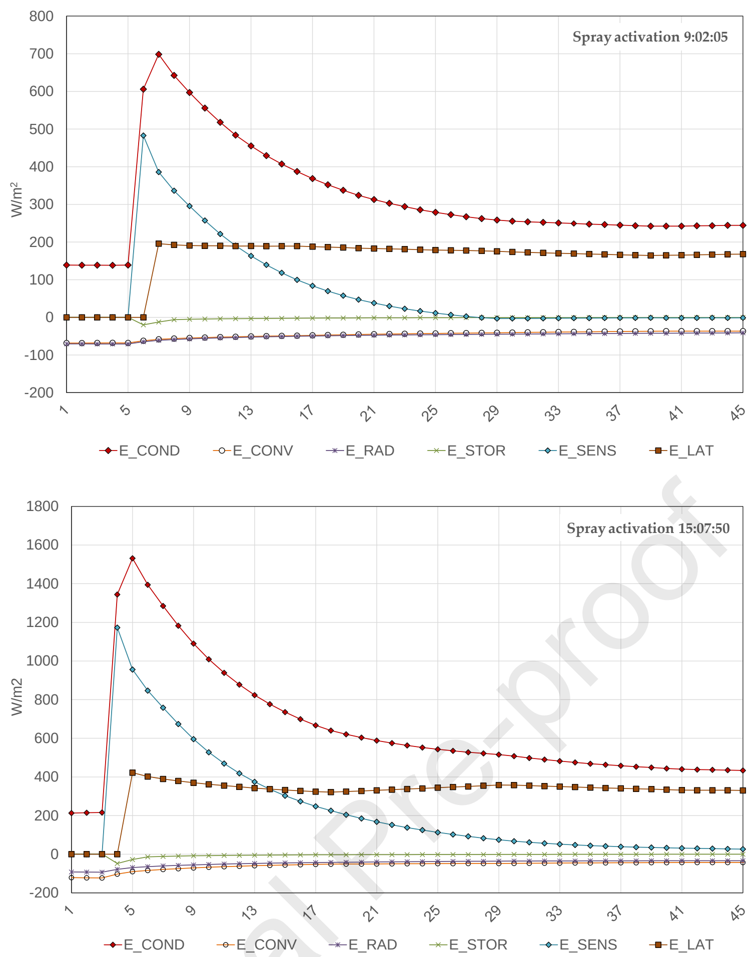

Fig. 8. Energy balance contributions of the back-surface node on 16th of July at two different times of spray activation

In both cases, the sensible contribution overcomes the latent one for a few timesteps, and after that, the latent term becomes predominant with a heat flux almost constant around 200 W/m^2 for the first spray and slightly lower than 400 W/ m^2 for the spray with a maximum cooling effect. The sensible heat transfer, being related, aside from the available water flow rate, to the temperature difference between the panel back surface and the film of water on it, swiftly tends to vanish (around 20 time-steps) because, after the initial dramatic rise, the water film tends to quickly reach thermal equilibrium with the panel surface. The latent heat transfer, instead, shows a more stable and prolonged trend since it is only related to the mass of water on the panel surface and disappears when this is exhausted because of the continuous evaporation.

The convective and radiative terms register almost equal values and show an almost flat trend for the greatest part of the day. They are consistently lower than the values detected in the case of the not-cooled PV panel with average values of 47 W/m^2 and 51 W/m^2 for the first spray and of 58 W/m^2 and 45 W/m^2 in the second case.

3.3. Comparison of the performance with a reference panel

An evaluation of the performances of the cooling system has been then performed by means of simulations with the validated model, comparing the results obtained for a cooled and a reference non-cooled PV panel.

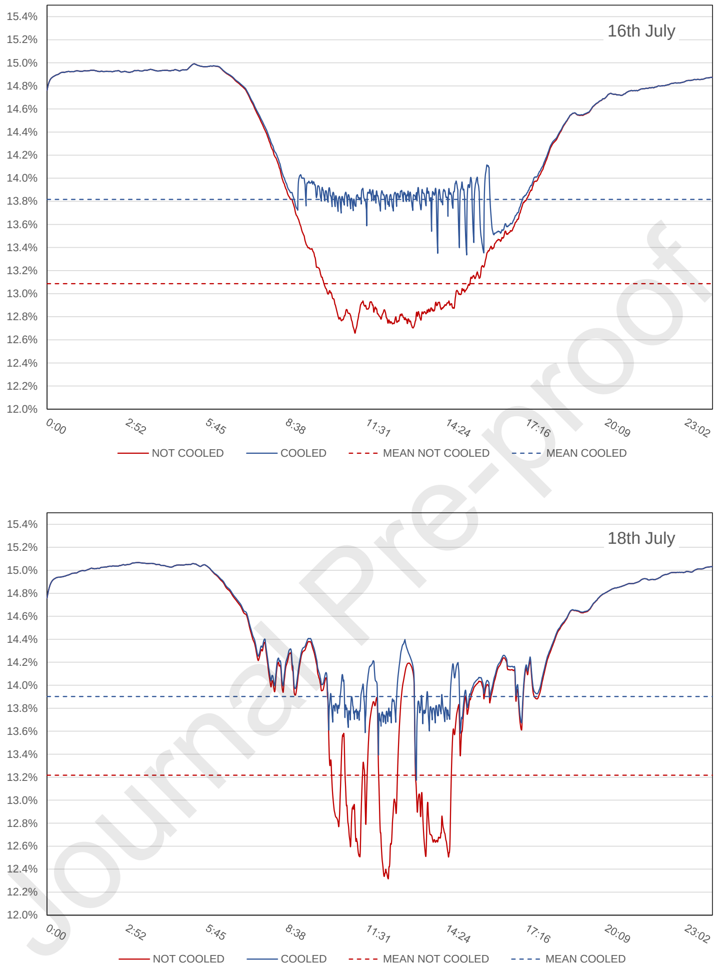

Fig. 9. Comparison of the efficiency between the case of uncooled module and the case of cooled module and their average values on a typical clear day a) and on a typical cloudy day b)

Fig. 9 reports a comparison between the daily pattern of the efficiency for the reference non-cooled module and for the cooled one on a clear day (16th July) and a cloudy day (18th July). Furthermore, the same graphs show the average values calculated in the time interval in which the cooling is active. In the clear day, there is an evident improvement in efficiency over a very long period (between 8:30 and 16:00). The average efficiency increases in both cases by 0.7 percentage points but with a maximum difference of 1.15 percentage points on a clear day and 1.44 percentage points on a cloudy day.

Fig. 10 shows the box plots representing the distributions of the average percentage differences of the hourly efficiencies (a) and percentage differences at midday (b) between the reference and the cooled module for different summer months

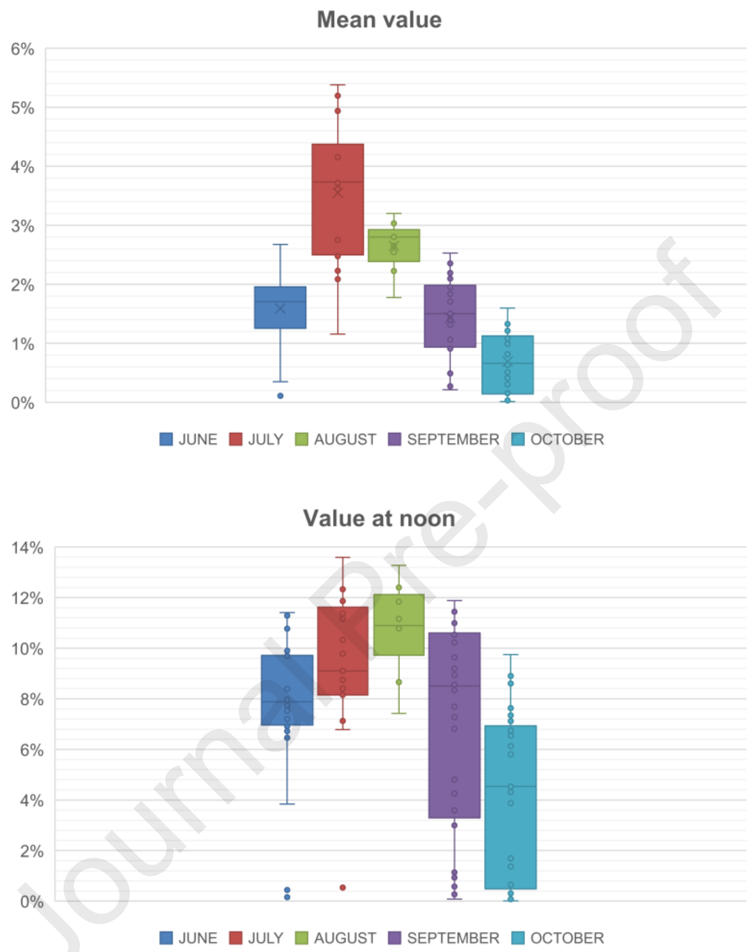

Fig. 10 Box plots representing the distributions of the average percentage differences of the efficiencies (a) and percentage differences at midday (b) between the reference and the cooled panel for different summer months

It can be observed how the benefit obtainable with the cooling system increases in hotter months with greater incident solar irradiation, reaching maximum increases of about 5.4% for the daily averages and about 12% at midday. The lower differences obtained in August are attributable to the scarcity of available climatic data for simulation, due to a temporary failure on the data acquisition system.

Furthermore, it is observed that in September and October there is a high dispersion of data with very low minimum values, mainly due to a high number of days with low temperatures, low irradiation, precipitation and adverse weather conditions that determine little increases from the cooling system. In any case, the results on efficiency suggest that the cooling system performs well in periods characterized by high air temperatures and solar irradiation, in which it is possible to obtain greater increases in the conversion efficiency.

A final analysis considered the energy required to produce the cooled PV module and the evaluation of the auxiliary energy needed to operate the cooling system. **Error! Reference source not found.** shows the cumulative monthly values of energy production for both the cooled and reference PV panel in the considered summer months. The table also reports the mean daily temperature of the cell surface. On a monthly basis, an evident gain from the use of the cooling system appears. The greatest increase of 2097.9 Wh is found in July, whereas the lowest of 860.3 Wh is observed in October. Furthermore, the cooling system was able to maintain a lower average daily PV cell temperature, with a maximum decrease of 4.80 °C in July, of about 3.62 °C in June and 3.26 °C in September.

In a precautionary manner the analysis considered the presence of a hydraulic pump with an electric nominal power of 1 kW, to guarantee the necessary pressure for an optimal spray also in localities in which specific conditions hinder an adequate level for spray cooling. The electrical consumptions of the pump are reported in Table 8**Error! Reference source not found.**, and are computed as the energy employed for the activation of the pump to produce the necessary pressure for the the spray operation time (5 s). The cumulative energy consumption is accounted considering the number of spray activation for each day. Even in the case of the employment of a hydraulic pump it is possible to obtain benefits from the cooling and therefore a positive net energy gain that reached the value of 1068.2 Wh in July.

Table 7. Monthly cumulative energy production and daily average cell temperature for the cooled (PV_cool) and the reference (PV_ref) panels in the different summer months

	Energy (Wh)				**Temperature (°C)**	
	PV_ref	**PV_cool**	**Pump**	**Net gain**	**PV_ref**	**PV_cool**
June	41366.8	43464.8	1196.0	901.9	28.9	25.3
July	42592.9	45387.0	1726.0	1068.2	32.4	27.6
September	32893.2	34633.3	1069.0	671.2	28.4	25.1
October	27087.6	27947.9	475.0	385.3	21.2	19.6

Finally, Table 8 reports the total and average monthly water consumption and the average daily number of activations of the spray. As it can be expected in hotter and more insolated months the PV module reaches a higher temperature and consequently the number of sprays increases as well as the total water consumption. To be noticed, however, that the particular nozzles chosen for cooling, employed with the available water network pressure of 3 bar allowed to obtain a very low value of water consumption, that did not exceed 0.5 m^3 in the worst case.

Table 8. Cumulative and average water consumption and average spray number in summer months

	JUNE	JULY	SEPTEMBER	OCTOBER
Tot water consume [m^3]	0.3396	0.4903	0.3037	0.1349
Mean water consume [m^3]	0.0113	0.0158	0.0105	0.0045
Mean spray number	29	40	27	11

4. Conclusions

Assessing the temperature and output power of the PV system is essential especially when cooling systems are applied. The literature has shown that water cooling is a very promising technique to lower the panel operative temperature, and in this context, spray cooling appears a simple, not expensive and effective system.

In order to be able to predict the thermal and electrical performances of spray-cooled PV modules, the study proposed a novel thermal model for PV panels equipped with a back surface spray cooling system. The latter was modeled after observing the phenomenon on an experimental setup located at the University of Calabria which allowed to collect data with a short sample time of 5 s on a PV panel equipped with two nozzles acting on the back surface. The 1-D thermal model was based on the energy balance method; the PV panel was discretized in 161 nodes where the general heat equation was approximated with an algebraic equation applying a Finite Difference (FD) method with an implicit time scheme, finally obtaining a system of algebraic equations which solution allowed to know the thermal field across the panel thickness. The model was then experimentally validated and used for an analysis of the phenomenon and the performance of the PV system. The results obtained are summarized below:

- An innovative methodology to model the term related to cooling appearing in the energy balance of the photovoltaic panel was proposed. The spray cooling model accounts for both sensible and latent heat extracted from the panel back surface, implementing a water mass balance at each time step, allowing add the cooling terms into the energy balance of the back surface node.
- The model was by data acquired over a long campaign of monitoring of an experimental set-up, using different statistical indexes to assess model results reliability. Although the complexity of the physical phenomena involved in the cooling process, the thermal model proved to be reliable in predicting the panel temperature with RSME that did not overcome 1.62 °C in July and August, and NSE values ranging from 0.934 to 0.9821. The errors proved to be even lower when predicting electric power with NSE ranging from 0.99834 to 0.9994, in the whole analyzed period, from July to October.

- A detailed analysis of the cooling phenomena highlighted the high values of exchanged sensible heat right after the spray, reaching the value of 1173 W/m^2 on a day of July, and that it swiftly tended to vanish after a few time-steps. The latent heat transfer, instead, showed a more stable and prolonged trend and disappeared after the complete evaporation of the water film on the panel back surface.
- The monthly water consumption from the cooling system is very low with a total monthly amount of 0.49 m^3 in July. Furthermore, the system was able to determine an energy increase of 2.8 kWh in July, with an average temperature drop of 4.8 °C. Even in the worst-case scenario of the adoption of a 1 kW pump to establish the required water pressure it is still possible to achieve net energy gain.

Acknowledgments

The research was partly supported by the Italian National Operational Programme (PON) through the project PON04a2_E “SINERGREEN e RES NOVAE - Smart Energy Master for the energy governance of the territory”.

Appendix A. Calculation of solar radiation on a tilted surface

The total solar radiation on a tilted surface G is the sum of three components, namely beam, diffuse and reflected radiation [34]:

$$G = G_b + G_d + G_r \tag{49}$$

The beam component is obtained from the beam radiation on the horizontal plane I_{b0} as follows [34]:

$$G_b = I_{b0} \cdot R_b = I_{b0} \cdot \frac{\cos i}{\sin \alpha} \tag{50}$$

where R_b is the beam tilt factor, i is the solar incidence angle and α is the solar altitude in the sky. Assuming the sky as an isotropic source of diffuse radiation, the diffuse component on the tilted surface is obtained from the diffuse radiation on the horizontal plane I_{d0} [34]:

$$G_d = I_{d0} \cdot R_d = I_{d0} \cdot \frac{1 + \cos \beta}{2} \tag{51}$$

where R_d is the diffuse tilt factor and β is the surface tilt angle. Finally, the reflected component is obtained from the sum of the beam and diffuse radiation as [34]:

$$G_r = (I_{b0} + I_{d0}) \cdot R_r = (I_{b0} + I_{d0}) \cdot \rho \cdot \frac{1 - \cos \beta}{2} \tag{52}$$

where R_r is the reflected tilt factor and ρ is the albedo of the surrounding surface.

Appendix B. Surface convective and radiative heat exchanges

The Nusselt number for natural convection for the specific configuration is given by [47]:

$$\mathrm{Nu}_{nat} = \begin{cases} 0.76 \cdot \mathrm{Ra}^{1/4} & \text{for } 10^4 < \mathrm{Ra} < 10^7 \\ 0.15 \cdot \mathrm{Ra}^{1/3} & \text{for } 10^7 \leq \mathrm{Ra} < 3 \cdot 10^{10} \end{cases} \tag{53}$$

where Ra is the Rayleigh number determined as the product between the Grashof (Gr) and the Prandtl (Pr) number [31]:

$$\mathrm{Gr} = \frac{\mathrm{g} \cdot \zeta_{\mathrm{air}} \cdot (\mathrm{T}_{\mathrm{surface}} - \mathrm{T}_{\mathrm{air}}) \cdot \mathrm{l}_{\mathrm{Ch}}^{3}}{\nu_{air}^{2}} \tag{54}$$

$$\Pr = \frac{\mathrm{c}_{air} \cdot \nu_{air} \cdot \rho_{air}}{\mathrm{k}_{\mathrm{air}}} \tag{55}$$

where ν_{air} is the air kinematic viscosity, c_{air} is the air specific heat capacity, k_{air} is the thermal conductivity of the air left constant to 0.026 W m^{-1}K^{-1}, g is the gravity acceleration, ζ_{air} is the volumetric coefficient of thermal expansion set to T_{film}^{-1}, T_{surf} is the PV (front or back) surface temperature, T_{air} is the ambient temperature and l_{ch} is the characteristic length of the PV panel, determined as [48]:

$$\mathrm{l}_{\mathrm{Ch}} = 4 \cdot \frac{\mathrm{A}_{\mathrm{Pan}}}{\mathrm{P}_{\mathrm{Pan}}} \tag{56}$$

The natural convection heat transfer coefficient is then obtained as [45]:

$$\mathrm{h}_{\mathrm{conv,nat}} = \frac{\mathrm{Nu}_{nat} \cdot \mathrm{k}_{\mathrm{air}}}{\mathrm{l}_{Ch}} \tag{57}$$

The Nusselt number for forced convection coefficient is given by [49]:

$$Nu_{for} = 0{,}86 \times Re^{1/2} \times Pr^{1/3} \tag{58}$$

where Prandtl number is obtained from Eq. (13) and Reynolds number Re is given by[45]:

$$Re = \frac{v_w \times I_{ch}}{\nu_{air}} \tag{59}$$

In the calculation of the convective heat exchange coefficient relating to forced convection, different methodologies were analyzed [50] and the most accurate was selected for the case in question.

Once Nu_{for} and Nu_{free} are calculated, the global Nusselt number Nu is determined according to the following cases as a function of the Archimede number [48]:

$Nu = Nu_{forc}$	$if\ Ar = \frac{\mathrm{Gr}_L}{Re_L^2} \leq 0.01$	Natural convection is neglected	(60)
$Nu = \sqrt[3]{Nu_{nat}^3 + Nu_{for}^3}$	$if\ 0.01 < Ar < 100$	Natural and forced convection are considered	(61)
$Nu = Nu_{nat}$	$if\quad \mathrm{Ar} > 100$	Forced convection is neglected	(62)

and then the total heat transfer coefficient can be obtained[45]:

$$h_{conv} = \frac{Nu \times k_{air}}{l_{ch}} \tag{63}$$

The linearized radiative heat transfer coefficient is obtained from the following expression, suggested to avoid numerical instabilities [39]:

$$h_{rad,surf-sink} = \frac{\sigma \cdot \left(T_{surf}^2 + T_{sink}^2\right) \cdot \left(T_{surf} + T_{sink}\right)}{\frac{1-\varepsilon_{surf}}{\varepsilon_{surf}} + \frac{1}{F_{surf-sink}}} \tag{64}$$

where σ is is the Stefan-Boltzmann constant, ϵ_{surf} is the emissivity of front/back surface of the PV panel, (ε_{gl} is set to 0.95 and ε_{ted} is set to 0.85), T_{surf} is the temperature of the front/back surface, T_{sink} is either the ground or sky temperature, and $F_{surf-sink}$ the view factors for radiation from any surface to the sky or ground. The view factors are defined as follow [31]:

$$\begin{gathered} \mathrm{F_{gl-sky}} = \frac{1}{2}(1 + \cos \beta) \\ \mathrm{F_{gl-ground}} = \frac{1}{2}(1 - \cos \beta) \\ \mathrm{F_{ted-sky}} = \frac{1}{2}[1 + \cos(\pi - \beta)] \\ \mathrm{F_{ted-ground}} = \frac{1}{2}[1 - \cos(\pi - \beta)] \end{gathered} \tag{65}$$

Appendix C. Thermodynamic properties of water and air

The specific heat, density and latent heat of vaporization of water are obtained from the following relationships, obtained by interpolation from tables of textbook [51]:

$$c_{p,water} = 3.0721617 \times 10^{-12} \times T_{water}^6 - 5.7980888 \times 10^{-9} \times T_{water}^5 + 4.5583002 \times 10^{-6} \times T_{water}^4 - 0.0019109851 \times T_{water}^3 + 0.45064221 \times T_{water}^2 - 56.68556 \times T_{water} + 2976.163 \quad (66)$$

$$\rho_{wat} = 1.4685559973 \times 10^{-9} \times T_{wat}^6 + 2.7421045035 \times 10^{-6} \times T_{wat}^5 + 2.1299003942 \times 10^{-3} \times T_{wat}^4 + 8.8085555312 \times 10^{-1} \times T_{wat}^3 + 2.0455700597 \times 10^{+2} \times T_{wat}^2 + 2.5289081167 \times 10^{+4} \times T_{wat} + 1.3012338754 \times 10^{+6} \quad (67)$$

$$\lambda = 2 \times 10^{-5} \times T_{water}^3 - 0{,}0032 \times T_{water}^2 - 2{,}2595 \times T_{water} + 2501 \quad (68)$$

The specific heat, density, thermal conductivity, dynamic viscosity and kinematic viscosity of air are obtained from the following relationships, obtained by interpolation from tables of textbook [51]:

$$c_{air} = -2 \times 10^{-8} \times T_{film}^4 + 3 \times 10^{-5} \times T_{film}^3 - 0{,}014 \times T_{film}^2 + 2{,}9674 \times T_{film} + 767{,}63 \quad (69)$$

$$k_{air} = \frac{0{,}026 \times T_{film}}{293{,}15} \quad (70)$$

$$\rho_{air} = -0{,}0039 \times T_{film} + 2{,}3419 \quad (71)$$

$$\mu_{air} = -3 \times 10^{-11} \times T_{film}^2 + 6 \times 10^{-8} \times T_{film} + 2 \times 10^{-6} \quad (72)$$

$$\nu_{air} = 9 \times 10^{-11} \times T_{film}^2 + 4 \times 10^{-8} \times T_{film} + 2 \times 10^{-6} \quad (73)$$

Appendix D. Comparison between the different sky models.

A comparison between the various formulation to calculate the sky was conducted to identify the most suitable one for the location considered in the study.

The experimental models proposed in the literature can be divided into direct models, in which the sky temperature can be directly determined as a function of the ambient temperature and air relative humidity, and models based on the emissivity coefficient of the sky ε_{sky}. In the latter case, the sky temperature is determined by [40]:

$$T_{sky} = \varepsilon_{sky}^{0,25} \times T_a \tag{74}$$

Some of the most relevant models, analyzed in the study, are reported below.

	Atmospheric emissivity models		
Eq.	**Model**	**Author**	**Ref.**
1	ε_{sky}=0.8004+0.00396·T_{dp}	Bliss	[40]
2	ε_{sky}=0.711+0.56·(T_{dp}/100) + 0.73·(T_{dp}/100)^2	Berdahl and Martin	
3	ε_{sky}=0.741+0.0062·T_{dp}	Berdahl and Fromberg	
4	ε_{sky}=0.77+0.0038·T_{dp}	Berger et al.	
5	ε_{sky}=0.787+0.764·log((T_{dp}+273.157) / 273)	Clarc and Allen	
6	ε_{sky}=0.34+0.11·$P_v^{0.5}$	Robitzsch	
7	ε_{sky}=0.48+0.058·$P_v^{0.5}$	Angstorm (Algeria)	
8	ε_{sky}=0.56+0.08· $P_v^{0.5}$	Centeno	[52]
	Direct temperature models		
9	T_{sky}=0.6·T_a	Alnaser	[41]
10	T_{sky}=0.0552·$T_a^{1.5}$	Swinbank	[40]
11	T_{sky}=T_a-20	Garg	

The following figure reports the results for a single day of July where the sky temperature was also obtained from experimental measurements of longwave radiation exchanged with the sky made by a pyrgeometer, assuming the sky as a black body according to [53]:

$$T_{sky} = \left(\frac{\phi}{\sigma}\right)^{0,25} \tag{75}$$

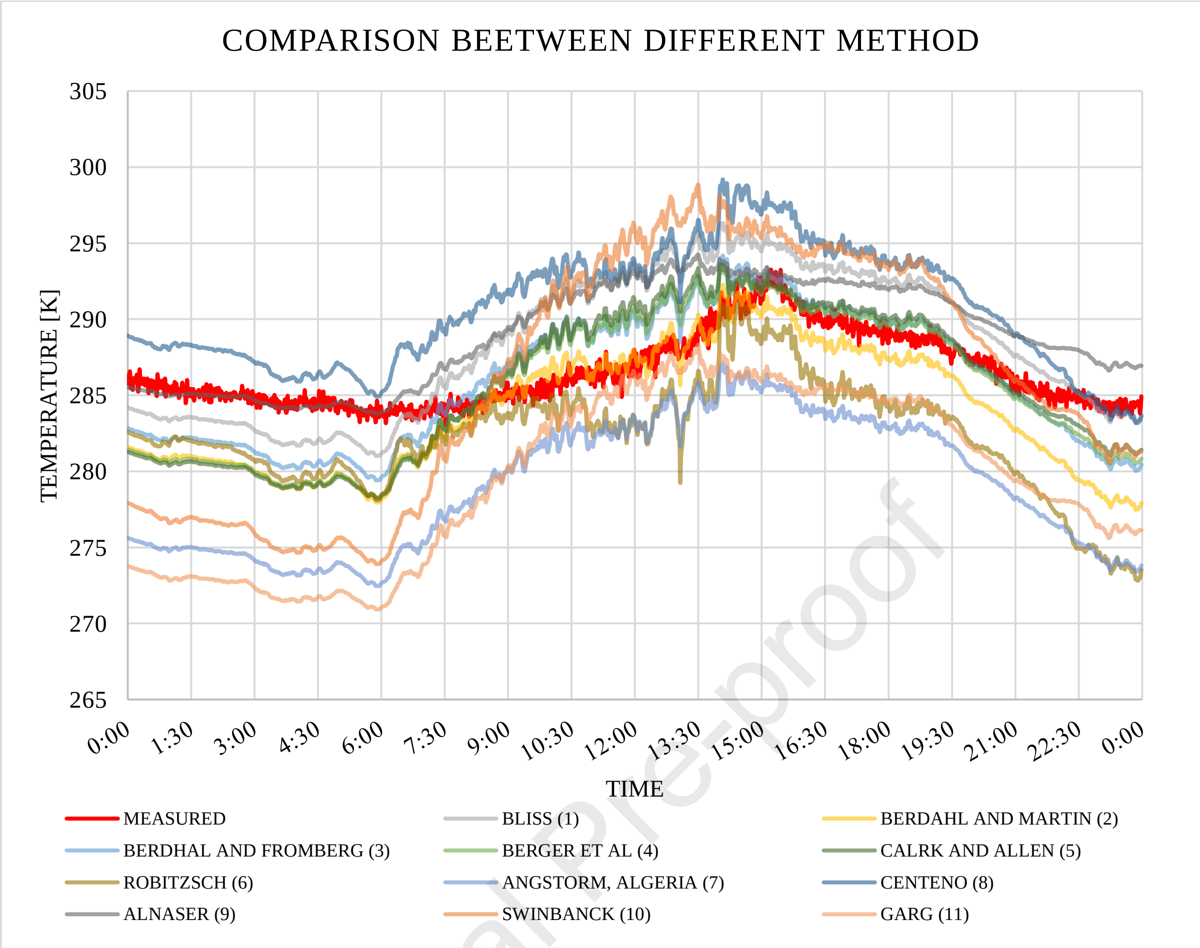

It can be seen that many models are unable to replicate adequately the trend of the measured sky temperature, while some show a certain accuracy only at certain times of the day. It should be noted that no one of the literature models is able to provide an accurate sky temperature for the specific climatic conditions considered. Such temperature can vary rapidly and is linked to complex and difficult atmospheric phenomena. After performing a series of preliminary simulations for different days the formulation proposed by Alnaser [41] was adopted since it was able to provide the highest correlation indexes for back surface temperature and electric power and was therefore considered as the most appropriate.

Appendix E. Evaluation of the evaporated water rate

The air saturation pressure at the film temperature is evaluated as:

$$p_{s,w} = 610{,}5 \times \exp\left[\frac{(17{,}269 \times T_{film})}{(237{,}7 + T_{film})}\right] \tag{76}$$

where T_{film} is the average between surface and water:

$$T_{film} = \frac{T_{surf} + T_w}{2} \tag{77}$$

The air vapor pressure is obtained from air relative humidity RH and air saturation pressure at air temperature $p_{s,a}$ [45]:

$$p_a = \frac{RH \times p_{s,a}}{100} \tag{78}$$

where $p_{s,a}$ is given by:

$$p_{s,a} = 610{,}5 \times \exp\left[\frac{(17{,}269 \times T_a)}{(237{,}7 + T_a)}\right] \tag{79}$$

Appendix F. Climate and meteorological data examined days

In the following are shown the trends of the climatic and meteorological quantities relating to the days previously analysed are reported.

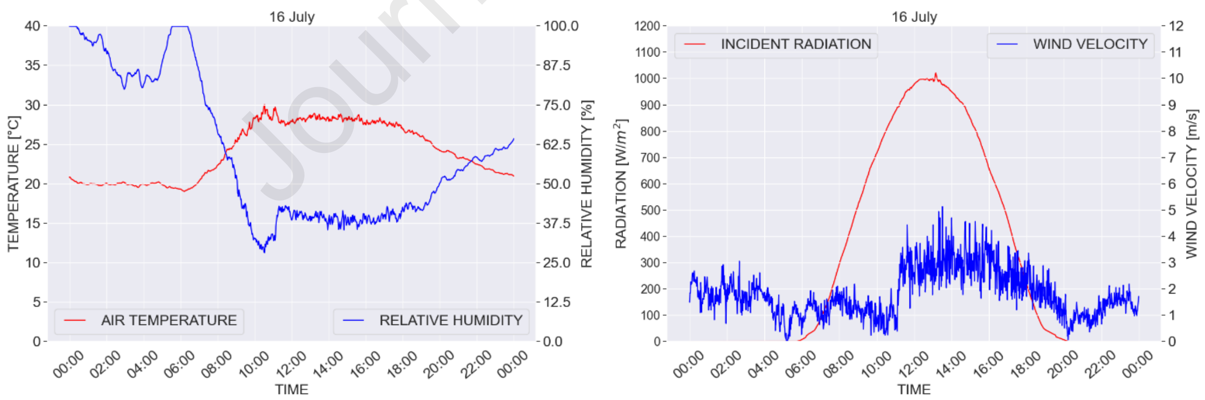

Experimental trends of air temperature, air relative humidity, wind velocity and incident radiation on the panel for 16th of July

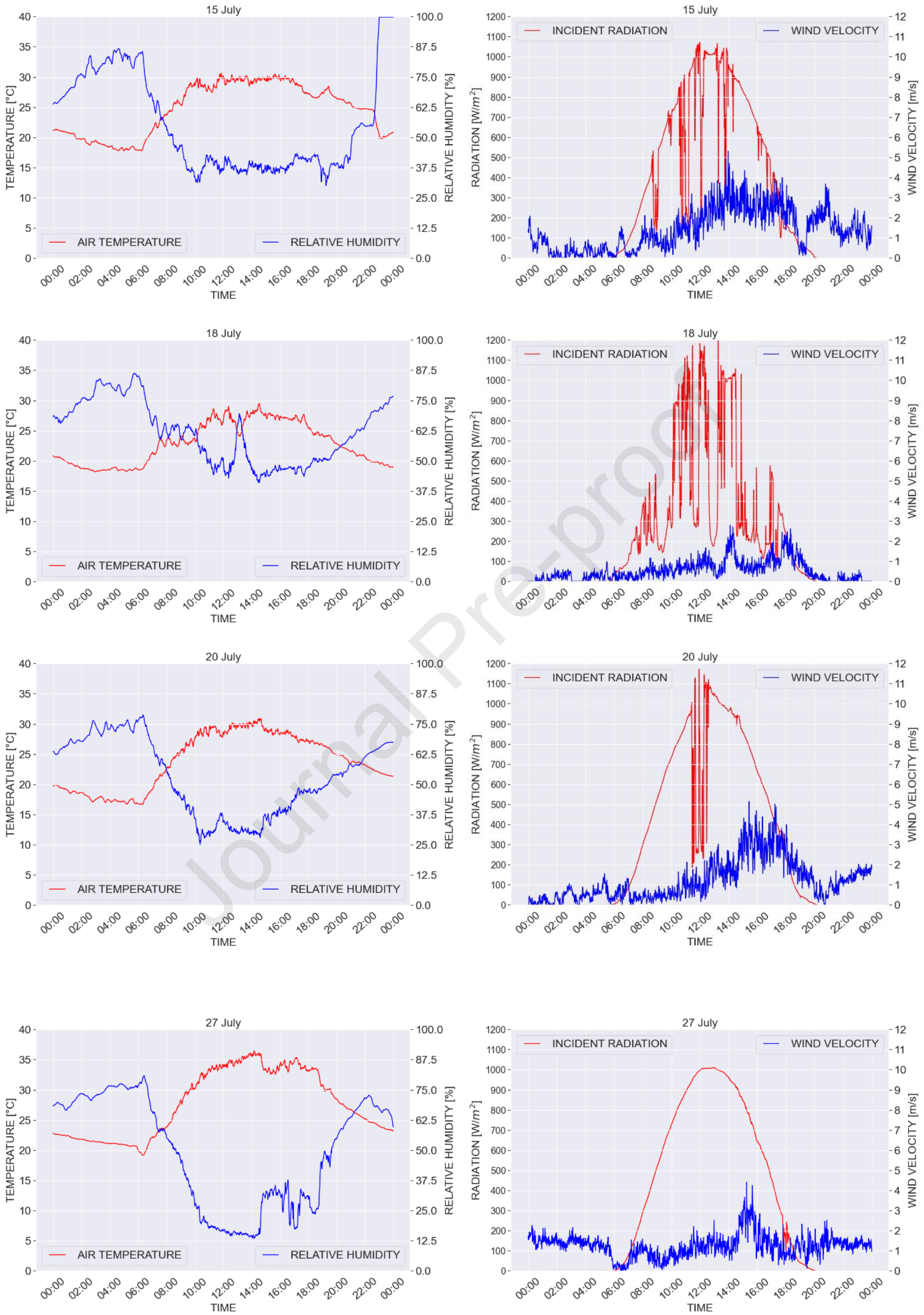
15 July
AIR TEMPERATURE
RELATIVE HUMIDITY
TEMPERATURE [°C]
RELATIVE HUMIDITY [%]
TIME
15 July
INCIDENT RADIATION
WIND VELOCITY
RADIATION [W/m²]
WIND VELOCITY [m/s]
TIME
18 July
AIR TEMPERATURE
RELATIVE HUMIDITY
TEMPERATURE [°C]
RELATIVE HUMIDITY [%]
TIME
18 July
INCIDENT RADIATION
WIND VELOCITY
RADIATION [W/m²]
WIND VELOCITY [m/s]
TIME
20 July
AIR TEMPERATURE
RELATIVE HUMIDITY
TEMPERATURE [°C]
RELATIVE HUMIDITY [%]
TIME
20 July
INCIDENT RADIATION
WIND VELOCITY
RADIATION [W/m²]
WIND VELOCITY [m/s]
TIME
27 July
AIR TEMPERATURE
RELATIVE HUMIDITY
TEMPERATURE [°C]
RELATIVE HUMIDITY [%]
TIME
27 July
INCIDENT RADIATION
WIND VELOCITY
RADIATION [W/m²]
WIND VELOCITY [m/s]
TIME

Experimental trends of air temperature, air relative humidity, wind velocity and incident radiation on the panel for selected days in July

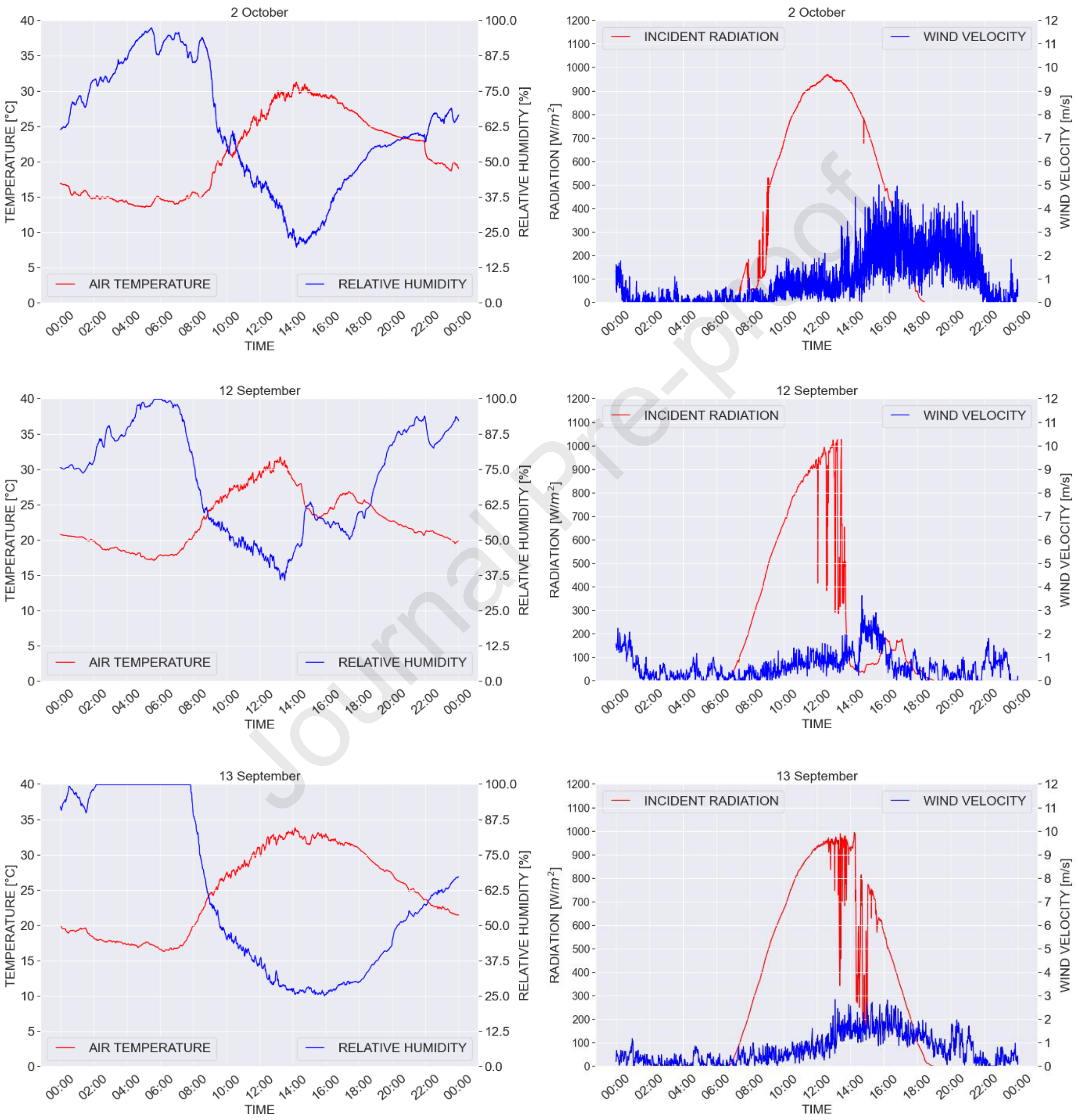

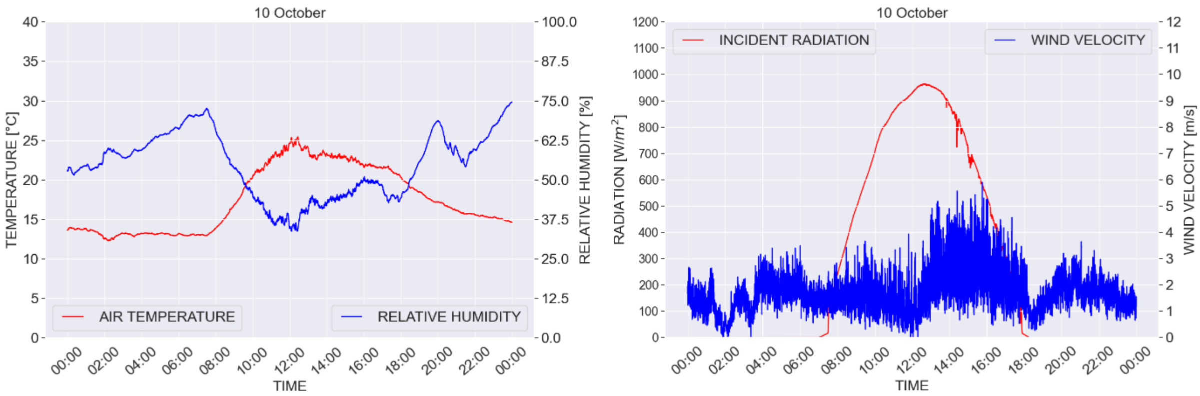

Experimental trends of air temperature, air relative humidity, wind velocity and incident radiation on the panel for selected days in September and October

References

[1] Settino J, Morrone P, Algieri A, Sant T, Micallef C, Farrugia M, et al. Integration of an Organic Rankine Cycle and a Photovoltaic Unit for Micro-Scale CHP Applications in the Residential Sector. Energy Procedia, 2017. doi:10.1016/j.egypro.2017.08.223.

[2] Cucumo MA, Ferraro V, Kaliakatsos D, Nicoletti F, Condò D. Thermal behaviour of a solar dish collector with flat mirrors using CFD analysis. Int J Heat Technol 2020;38:767–74. doi:10.18280/ijht.380401.

[3] Al-Amayreh MI, Alahmer A, Manasrah A. A novel parabolic solar dish design for a hybrid solar lighting-thermal applications. Energy Reports 2020. doi:10.1016/j.egyr.2020.11.063.

[4] Ferraro V, Marinelli V, Settino J, Nicoletti F. Techno-economic analysis of a solar tower power plant with an open air brayton cycle and a combined cycle - A simplified calculation method. Int J Heat Technol 2020;38:590–600. doi:10.18280/IJHT.380303.

[5] Cucumo MA, Ferraro V, Kaliakatsos D, Nicoletti F. Study of kinematic system for solar tracking of a linear Fresnel plant to reduce end losses. Eur J Electr Eng 2019. doi:10.18280/ejee.210501.

[6] Cucumo MA, Ferraro V, Kaliakatsos D, Mele M, Nicoletti F. Linear Fresnel plant with primary reflectors movable around two axes. Adv Model Anal A 2018. doi:10.18280/ama_a.550301.

[7] Algieri A, Morrone P, Bova S. Techno-Economic Analysis of Biofuel, Solar and Wind Multi-Source Small-Scale CHP Systems. Energies 2020, Vol 13, Page 3002 2020;13:3002. doi:10.3390/EN13113002.

[8] Morrone P, Algieri A. Integrated Geothermal Energy Systems for Small-Scale Combined Heat and Power Production: Energy and Economic Investigation. Appl Sci 2020, Vol 10, Page 6639 2020;10:6639. doi:10.3390/APP10196639.

[9] Aneli S, Gagliano A, Tina GM, Gediz Ilis G, Demir H. Effectiveness and constraints of using PV/Thermal collectors for heat-driven chillers. Appl Therm Eng 2022;210:118330. doi:10.1016/J.APPLTHERMALENG.2022.118330.

[10] Settino J, Sant T, Micallef C, Farrugia M, Spiteri Staines C, Licari J, et al. Overview of solar technologies for electricity, heating and cooling production. Renew Sustain Energy Rev 2018. doi:10.1016/j.rser.2018.03.112.

[11] Marino C, Nucara A, Panzera MF, Pietrafesa M, Pudano A. Economic Comparison Between a Stand-Alone and a Grid Connected PV System vs. Grid Distance. Energies 2020, Vol 13, Page 3846 2020;13:3846. doi:10.3390/EN13153846.

[12] Nicoletti F, Cucumo MA, Ferraro V, Kaliakatsos D, Settino J. Performance analysis of a double-sided PV plant oriented with backtracking system. Math Model Eng Probl 2020;7:325–34. doi:10.18280/MMEP.070301.

[13] Telichenko V, Benuzh A, Eames G, Orenburova E, Shushunova N. Development of Green Standards for Construction in Russia. Procedia Eng., 2016. doi:10.1016/j.proeng.2016.08.233.

[14] Gattuso D, Greco A, Marino C, Nucara A, Pietrafesa M, Scopelliti F. Sustainable mobility: Environmental and economic analysis of a cable railway, powered by photovoltaic system. Int J Heat Technol 2016;34:7–14. doi:10.18280/IJHT.340102.

[15] Marino C, Nucara A, Panzera MF, Pietrafesa M. Towards the nearly zero and the plus energy building: Primary energy balances and economic evaluations. Therm Sci Eng Prog 2019;13:100400. doi:10.1016/J.TSEP.2019.100400.

[16] Gagliano A, Nocera F, Detommaso M, Evola G. Thermal Behavior of an Extensive Green Roof: Numerical Simulations and Experimental Investigations. Int J Heat Technol 2016. doi:10.18280/ijht.34S206.

[17] Tina GM, Scavo FB, Aneli S, Gagliano A. Assessment of the electrical and thermal performances of building integrated bifacial photovoltaic modules. J Clean Prod 2021;313:127906. doi:10.1016/J.JCLEPRO.2021.127906.

[18] Gagliano A, Tina GM, Aneli S, Chemisana D. Analysis of the performances of a building-integrated PV/Thermal system. J Clean Prod 2021;320:128876. doi:10.1016/J.JCLEPRO.2021.128876.

[19] Evola G, Margani G. Renovation of apartment blocks with BIPV: Energy and economic evaluation in temperate climate. Energy Build 2016. doi:10.1016/j.enbuild.2016.08.085.

[20] Manasrah A, Al Zyoud A, Abdelhafez E. Effect of color and nano film filters on the performance of solar photovoltaic module. Energy Sources, Part A Recover Util Environ Eff 2021. doi:10.1080/15567036.2019.1631907.

[21] Hamdan M, Brawiesh AK. Enhancement of PV performance using optical solar spectrum

splitting. Https://DoiOrg/101080/1556703620191668087 2019;43:2000–7. doi:10.1080/15567036.2019.1668087.

[22] Hudișteanu SV, Țurcanu FE, Cherecheș NC, Popovici CG, Verdeș M, Huditeanu I. Enhancement of PV Panel Power Production by Passive Cooling Using Heat Sinks with Perforated Fins. Appl Sci 2021, Vol 11, Page 11323 2021;11:11323. doi:10.3390/APP112311323.

[23] Jafari R. Optimization and energy analysis of a novel geothermal heat exchanger for photovoltaic panel cooling. Sol Energy 2021;226:122–33. doi:10.1016/J.SOLENER.2021.08.046.

[24] Sivakumar B, Navakrishnan S, Menaka &, Cibi R, Senthil R. Experimental study on the electrical performance of a solar photovoltaic panel by water immersion n.d. doi:10.1007/s11356-021-15228-z/Published.

[25] Evola G, Marletta L. Exergy and thermoeconomic optimization of a water-cooled glazed hybrid photovoltaic/thermal (PVT) collector. Sol Energy 2014. doi:10.1016/j.solener.2014.05.041.

[26] Manasrah AA, Alkhalil S, Masoud M. Investigation of multi-way forced convective cooling on the backside of solar panels. Int J Energy Convers 2020. doi:10.15866/irecon.v8i5.19516.

[27] Salkuti R, Manasrah A, Masoud M, Jaradat Y, Bevilacqua P. Investigation of a Real-Time Dynamic Model for a PV Cooling System. Energies 2022, Vol 15, Page 1836 2022;15:1836. doi:10.3390/EN15051836.

[28] Bevilacqua P, Morabito A, Bruno R, Ferraro V, Arcuri N. Seasonal performances of photovoltaic cooling systems in different weather conditions. J Clean Prod 2020. doi:10.1016/j.jclepro.2020.122459.

[29] Bevilacqua P, Perrella S, Cirone D, Bruno R, Arcuri N. Efficiency Improvement of Photovoltaic Modules via Back Surface Cooling. Energies 2021, Vol 14, Page 895 2021;14:895. doi:10.3390/EN14040895.

[30] Han X, Wang Y, Zhu L. Electrical and thermal performance of silicon concentrator solar cells immersed in dielectric liquids. Appl Energy 2011. doi:10.1016/j.apenergy.2011.05.037.

[31] Bevilacqua P, Bruno R, Arcuri N. Comparing the performances of different cooling strategies

to increase photovoltaic modules electric in different meteorological conditions. Energy 2020;195:116950. doi:10.1016/j.energy.2020.116950.

[32] Benato A, Stoppato A, Vanna F De, Schiro F. Spraying Cooling System for PV Modules: Experimental Measurements for Temperature Trends Assessment and System Design Feasibility. Des 2021, Vol 5, Page 25 2021;5:25. doi:10.3390/DESIGNS5020025.

[33] Zilli BM, Lenz AM, de Souza SNM, Secco D, Nogueira CEC, Junior OHA, et al. Performance and effect of water-cooling on a microgeneration system of photovoltaic solar energy in Paraná Brazil. J Clean Prod 2018. doi:10.1016/j.jclepro.2018.04.241.

[34] Osma-Pinto G, Ordóñez-Plata G. Measuring the effect of forced irrigation on the front surface of PV panels for warm tropical conditions. Energy Reports 2019. doi:10.1016/j.egyr.2019.04.010.

[35] Castanheira AFA, Fernandes JFP, Branco PJC. Demonstration project of a cooling system for existing PV power plants in Portugal. Appl Energy 2018. doi:10.1016/j.apenergy.2017.11.086.

[36] Notton G, Cristofari C, Mattei M, Poggi P. Modelling of a double-glass photovoltaic module using finite differences. Appl Therm Eng 2005. doi:10.1016/j.applthermaleng.2005.02.008.

[37] Aly SP, Ahzi S, Barth N, Abdallah A. Using energy balance method to study the thermal behavior of PV panels under time-varying field conditions. Energy Convers Manag 2018. doi:10.1016/j.enconman.2018.09.007.

[38] Aly SP, Barth N, Figgis BW, Ahzi S. A fully transient novel thermal model for in-field photovoltaic modules using developed explicit and implicit finite difference schemes. J Comput Sci 2018. doi:10.1016/j.jocs.2017.12.013.

[39] Marwaha S, Pratik P, Ghosh K. Thermal Model of Silicon Photovoltaic Module with Incorporation of CFD Analysis n.d. doi:10.1007/s12633-021-01184-3.

[40] Yaman K, Arslan G. A detailed mathematical model and experimental validation for coupled thermal and electrical performance of a photovoltaic (PV) module. Appl Therm Eng 2021;195:117224. doi:10.1016/J.APPLTHERMALENG.2021.117224.

[41] Nižetić S, Grubišić- Čabo F, Marinić-Kragić I, Papadopoulos AM. Experimental and numerical investigation of a backside convective cooling mechanism on photovoltaic panels. Energy 2016. doi:10.1016/j.energy.2016.05.103.

[42] Salameh T, Tawalbeh M, Juaidi A, Abdallah R, Hamid AK. A novel three-dimensional numerical model for PV/T water system in hot climate region. Renew Energy 2021;164:1320–33. doi:10.1016/J.RENENE.2020.10.137.

[43] Moharram KA, Abd-Elhady MS, Kandil HA, El-Sherif H. Enhancing the performance of photovoltaic panels by water cooling. Ain Shams Eng J 2013. doi:10.1016/j.asej.2013.03.005.

[44] Nižetić S, Čoko D, Yadav A, Grubišić-Čabo F. Water spray cooling technique applied on a photovoltaic panel: The performance response. Energy Convers Manag 2016. doi:10.1016/j.enconman.2015.10.079.

[45] Hadipour A, Rajabi Zargarabadi M, Rashidi S. An efficient pulsed- spray water cooling system for photovoltaic panels: Experimental study and cost analysis. Renew Energy 2021;164:867–75. doi:10.1016/J.RENENE.2020.09.021.

[46] Osma-Pinto G, Ordóñez-Plata G. Dynamic thermal modelling for the prediction of the operating temperature of a PV panel with an integrated cooling system. Renew Energy 2020;152:1041–54. doi:10.1016/J.RENENE.2020.01.132.

[47] Shahverdian MH, Sohani A, Sayyaadi H. Water-energy nexus performance investigation of water flow cooling as a clean way to enhance the productivity of solar photovoltaic modules. J Clean Prod 2021;312:127641. doi:10.1016/J.JCLEPRO.2021.127641.

[48] Bevilacqua P, Perrella S, Bruno R, Arcuri N. An accurate thermal model for the PV electric generation prediction: Long-term validation in different climatic conditions. Renew Energy 2020. doi:10.1016/j.renene.2020.07.115.

[49] Duffie JA, Beckman WA. Solar Engineering of Thermal Processes: Fourth Edition. 2013. doi:10.1002/9781118671603.

[50] Notton G, Cristofari C, Mattei M, Poggi P. Modelling of a double-glass photovoltaic module using finite differences. Appl Therm Eng 2005;25:2854–77. doi:10.1016/j.applthermaleng.2005.02.008.

[51] Çengel Y a. Thermodynamics: An Engineering Approach. McGraw-Hill 2004.

[52] Oliveti G, Marletta L, Arcuri N, De Simone M, Bruno R, Evola G. Solar energy. Green Energy Technol., 2014. doi:10.1007/978-3-319-03074-6_4.

[53] Incropera FP, DeWitt DP, Bergman TL, Lavine AS. Fundamentals of Heat and Mass Transfer(6th edition). 2007. doi:10.1016/j.applthermaleng.2011.03.022.

[54] Aigarni S, Nutter D. Survey of sky effective temperature models applicable to building envelope radiant heat transfer. ASHRAE Conf 2015;121:351–63. doi:10.13140/RG.2.1.4212.5526.

[55] Alnaser WE. Estimation of the clear sky and the ground emissivity in Bahrain. Earth, Moon Planets 1990;48:177–81. doi:10.1007/BF00054101.

[56] Oliphant K, Webb BW, McQuay MQ. An experimental comparison of liquid jet array and spray impingement cooling in the non-boiling regime. Exp Therm Fluid Sci 1998;18:1–10. doi:10.1016/S0894-1777(98)10013-4.

[57] Rybicki JR, Mudawar I. Single-phase and two-phase cooling characteristics of upward-facing and downward-facing sprays. Int J Heat Mass Transf 2006;49:5–16. doi:10.1016/J.IJHEATMASSTRANSFER.2005.07.040.

[58] Shah MM. Methods for calculation of evaporation from swimming pools and other water surfaces. ASHRAE Trans 2014;120:3–18.

[59] Kline M. Describing uncertainities in single sample. Mech Eng 1953;75:3–8.

A novel thermal model including spray cooling for PV panels was proposed

The model was validated with experimental data

An accurate analysis of the cooling phenomena was conducted

The average efficiency in summer increased by 5.4 %

Declaration of interests

☒ The authors declare that they have no known competing financial interests or personal relationships that could have appeared to influence the work reported in this paper.

☐The authors declare the following financial interests/personal relationships which may be considered as potential competing interests: